Discrete track electrodynamic maglev Part I: Modelling

Ove F Storset[1] and Bradley E Paden
Mechanical and Environmental Engineering Department,
University of California, Santa Barbara,
CA 93106-5070, U.S.A.
Email[1]: ove.storset@ieee.org

September 30, 2005

Abstract

Since the dawn of maglev transportation technology in the 1970's, a great variety of models for electrodynamic suspension (EDS) magnetic levitation (maglev) have been presented. This article unifies these models by deriving equations for discrete track EDS maglev (with stranded or solid conductors), and introduces criteria required to justify the approximation of track currents by current filaments. Parallels to the diffusion equation governing continuous tracks are also provided. Our EDS analyses are careful to clarify the validity of the modelling assumptions, and strive to maintain accurate static and dynamic properties in the reduced order equations. The development starts with the derivation of a general diffusion equation (with source) describing the evolution of current fields in an arbitrary track. We then simplify the track current fields to filaments reducing the Laplacian in the diffusion equation to a discrete convolution operator. The final result, the key contribution of this paper, is an infinite-dimensional model that can be truncated to an ODE for numerical evaluation that yields accurate predictions of dynamic stability. In addition, the infinite-dimensional model is amenable to harmonic analysis and, hence, the computation of lift, drag and other static properties. Although we derive a 2DOF (heave, propulsion) model, the modelling approach applies to 6DOF systems.

1 Introduction

This investigation focuses on electrodynamic suspension (EDS) magnetic levitation (maglev), where a repulsive levitation force is created between a moving magnetic source and currents induced in a conductive guideway. This is distinct from the technologically more mature electromagnetic suspension, where forces are generated between a source magnetic field and a ferromagnetic guideway [1],[2].

Modeling EDS maglev dates back to Maxwell's current-sheet model of a magnet above a rotating metallic disc—Arago's disc in Chapter XII of [3]. Subsequently, in the early 1900's, maglev largely consisted of devices on drawing boards, patents, or science fiction; all relying on unborn technology.

Further progress did not arrive before the early 1960's when development of low temperature superconductors (SC) inspired two visionary researchers at Brookhaven National Laboratory, Powell and Danby, to invent the null-flux levitation concept[1] and to promote SC maglev as the mass transportation of the future [5]-[8]. In the early seventies, the world caught on, and there was a "gold rush" to develop maglev transportation technology in Germany [9],[10]; United States [11],[12]; Japan [13]; Canada [14]; and Great Britain [15]. By the late seventies, the momentum had stagnated due to immature superconductor, power electronics, and cryogenics technology in addition to the physical complexity of SC EDS. Electrodynamic suspension research programs were discontinued all over the world, except in Japan, where it took a significant blow with the recession in the 1980's. In spite of this, the Japanese Railway Technical Research Institute (RTRI) [16] has succeeded in developing a reliable high-speed transportation technology for deployment in the Tokyo-Osaka corridor, but there are remaining cost and performance issues [17].

For a long time, SC magnets were deemed the only viable magnetic source for EDS as permanent magnets (PM) had poor weight efficiency. However, with the arrival of Neodymium-Iron-Boron (NdFeB) magnets [18] and improved production technology [19] in the eighties, PM EDS levitation became technologically feasible.

Mallinson's discovery of magnet geometries with one-sided fluxes [20],[21], focusing the magnetic field towards the track, simultaneous with Halbach's similar invention of PM arrays used in "wigglers" for free electron lasers [22]-[24], produced PM EDS with a much shorter pole pitch than SC EDS, and lowered the lift-off velocity to walking speed without complex cryogenics. Researchers at Lawrence Livermore National Laboratory (LLNL), first funded by NASA for developing electromagnetic rocket launchers [25]-[27], exploited these inventions in the "Inductrack" system. Later, Post at LLNL combined Halbach arrays with the "hybrid null-flux" concept [28] and ladder tracks to improve the lift-to-drag ratio. Post thereby extended EDS maglev to the hitherto unconceived application of low-speed urban mass transport [29].

Post's "Inductrack" technology has been adopted by the Federal Transit Administration in their Urban Magnetic Levitation Transit Technology Development Program where General Dynamics is the prime contractor [30],[31]. Shortly, a prototype will be deployed at California University in Pennsylvania [32].

Despite maglev's failure to swiftly fulfill the expectations of the 1970's, it is still the transport technology for the future due to the combination of energy efficiency, environmental friendliness, and high speed. As Moon points out in [33], it took nearly 70 years from the time the Wright brothers made their first powered flight in 1903 until the commercial success of air travel in the 1970's. Maglev is not different. We claim that EDS maglev's delayed success is partly caused by premature development with insufficient basic research addressing the complexity of underlying physics. The modelling efforts in this paper represents our response to the need for basic research in EDS.

Electrodynamic suspension maglev is an intricate technology involving nonlinear bifurcating dynamics, superconductor quenching, and 3D current diffusion—rocket science if you like—which requires some attention to detail. For some time maglev models for transportation have been developed using existing electric machine theory which leads to over-simplifications and conceals possible solutions. Our research is motivated by the need to refine the present models.

There is a specific need for improved models for several reasons: **i**) The general structure unifying all EDS must be utilized to define principles that help make sense of experimental successes and failures. Identical concepts are sometimes treated with different and unreconciled models despite simple relationships. Some examples are:

[1] Initially, in their spare time as the transport community viewed their proposal more with amusement than with genuine interest, and the scientific community had neither the interest nor the funding [4], p. 48.

[34] and [35] on thin track theory, [36] and [37] on heave dynamics, [28] and [29] on the null-flux concept. **ii**) We need models that convey overreaching relationships amongst key parameters. In contrast, FEM is a powerful tool for analysis, but less applicable for synthesis. **iii**) Efficient cost optimized designs rely on accurate parametric models. Otherwise, numerical optimization algorithms might reduce actual performance instead of improving it. Two elementary examples are the recommendation to increase conductor thickness to boost the lift-to-drag ratio in [38] based on a model that excludes eddy currents, or the overly optimistic lift-to-drag ratio (>200) in [25] also predicted without eddy current models. **iv**) The shortcomings of "generalized electric machine theory" with filament currents[2] and lumped parameters to describe dynamic behavior. The theory is traditionally utilized in electric machine design, but is relabeled "impedance modelling" in association with maglev [39]-[44]. There are several examples of approximate dynamic assessments with disagreement between theory and experiment [41],[45],[37]. Well-behaved dynamic experiments, caused by unmodelled resistive or mechanical losses that in general—but not always—damp oscillatory motions, are conceived as experimental corroboration of invalid stability arguments. An example is Powell and Danby's [8] invalid Lyapunov argument neglecting the nonconservative drag force caused by resistive losses. This force can cause dynamic instability as explained by Moon in [33], Chapter 5.

In addition, dynamic instability is commonly overlooked as in [46],[40],[47]. We emphasize that restoring forces at an equilibrium are not sufficient for stability[3].

1.1 Literature review on EDS models

Electrodynamic levitation is traditionally categorized into *continuous track* systems made of homogenous sheets of conducting material, and *discrete track* systems typified by those shown in Figure 1. There is a further

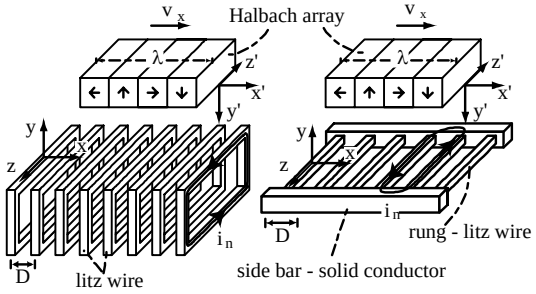

Figure 1: Examples of discrete track systems. Window framed track (left) and ladder track (right), both employ normal flux with a Halbach array source.

distinction between *null-flux* systems, utilizing flux cancellation at a center position in the source field with zero resulting levitation force, and increased stiffness, (labeled "hybrid null-flux" in [28], "flux cancelling EDS" in [49] and "null-current" in [29]), and e.m.f. cancellation at a center position in the track as Powell and Danby's original idea [5]. These are opposed to *normal-flux* systems, where there is no center position nor flux cancellation[4]. The track and flux types for levitation also applies to the guidance system with a corresponding multitude of possible system arrangements.

In applying Maxwell's equations, discrete tracks differ from the continuous ones only in the spatial dependency of the track resistivity $\rho(\mathbf{p})$, which is invariant to displacements in the propulsion direction in continuous tracks and periodic under the same displacements in discrete tracks. As continuous tracks can be viewed as generalizations of discrete tracks, it is appropriate to briefly review continuous track research.

[2] A filament current flows in an infinitely thin conductor. This is the type of current model used in electric circuit analysis.

[3] In EDS maglev, the non-conservative drag force can cause growing amplitude oscillations perpendicular to the direction of motion. The issue of stability of EDS is delicate, and must be approached with care [33], Chapter 5, [48].

[4] A third flux cathegory is *break-flux*, coined in [50], used to increase the drag force for breaking.

1.1.1 Continuous tracks

Continuous tracks were initially modelled with Maxwell's thin track theory [3], Chapter 12, that is powerful for building intuition, but the theory is less applicable for quantitative assessments. See [51] for a detailed review. A classic on "semi-quantitative calculations" is [28], but beware of ignoring the lateral spatial wave number k_y of the source. This is equivalent to assuming a source wavelength in the propulsion direction much shorter than the source width, which is rarely the case [52].

When the source magnetic field is a SC, it is customary to ignore back e.m.f. from the track justified by the shielding of the cryostat. However, this is not fully justified [53],[54].

In a non-relativistic setting, ignoring displacement current, Maxwell's equations reduce to a field diffusion equation governing the track current of EDS. The earliest works [55],[56] exploit the parallel to geometrical optics with a 2D Fourier formalism, made possible by the infinitely wide tracks having no vertical track current. This 2D setting is used in the extensive work by the research group of Siemens and includes modelling [50], experimental validation [57] and simplifications under various asymptotic conditions [52]. Not before after the heydays in the seventies, were the "mathematical fog" of geometrical optics removed with more general Green's function theory [58] providing valuable intuition. As Green's functions are harder to find for more complex track geometries, the method is not recommended for finite width tracks, and a purely numerical approach is inevitable. This was first done for a two dimensional source in [59], confirming a transverse destabilizing force with experimental corroboration in [60], but intuition is again lost in the numerics.

All these works solve the diffusion equation at constant levitation height and constant propulsion speed. A slight generalization allows rectilinear acceleration at constant levitation height [61] and reveals hysteresis cycles in the lift and drag forces versus velocity. Analyzing even more general motion, as specified by dynamic equations (e.g. heave), is an open research topic, and is likely to reveal bifurcations and periodic structures as our work suggests. It is also expected to replace the simple static force dependence versus velocity with dynamic equations.

The number of open problems in continuous track theory contributed to the discontinuation of the German EDS program [62] as their research to that point in time had not yet incorporated complete stability assessments [45]. Overlooking the importance of heave velocity in the damping term is commonly done as pointed out in [36].

1.1.2 Discrete tracks

For discrete tracks the distributed parameter nature of Maxwell's equations is also important, but approximation with filament currents is often made haphazardly, oftentimes neglecting eddy losses. For this reason, the discrete track theory is even less complete than that for continuous tracks, despite the tremendous development efforts undertaken by the Japanese RTRI on discrete tracks [16].

Powell and Danby's original papers [5],[8] had a strong promotional character, and the "semi-quantitative calculations" in [28], still surpass the precision offered in many contemporary articles. Early research at Stanford Research Institute (SRI) (later funded by U.S. Department of Transportation) [63],[64] outlines models for discrete tracks using lumped inductances and a spatial Fourier transform in the propulsion direction. A lumped parameter impedance model is developed, and the track currents are solved numerically. Although the SRI group exceeds most later publications in analysis tools, in reducing Maxwell's equations to linear circuit theory, the approximations made oversimplify the track physics.

Early research at Toshiba reproduced the lumped parameter impedance of the track from [63], and showed the superior lift-to-drag (L/D) ratio of ladder tracks [65]. Their research also indicated that for sufficiently long ground coils, the mutual inductance between track loops could be ignored [66]. In spite of their results, the Toshiba group produced rudimentary models, oftentimes with a number of questionable assumptions, like ignoring source end effects and higher order harmonics in [67].

Applying similar models and using numerical techniques, investigations undertaken at Grumman Aerospace [38] demonstrated that alternating polarity sources yield higher lift force than non-alternating, but the lack of physical reasoning and eddy current loss modelling lead to incorrect conclusions regarding conductor size and L/D optimization. An important experiment [68], in this regard, is reported from RTRI on the so called "zero-sag" eddy current drag, from finite conductor thickness in null-flux coils, combined with inductive loading

to increase lift-to-drag ratio. The eddy current losses created a maximum in the L/D-ratio versus propulsion velocity followed by a roll-off, limiting the L/D-ratio achievable with inductive loading.

Later research has been numerically oriented, applying linear circuit analysis with lumped parameters, with little explanation of the implications of the assumptions. The first model of the vehicle series developed by RTRI, is a numerical experiment for the ML-500 vehicle [69] later operated at the Miyasaki test track. The authors expand the source magnetic field in 2D Fourier series, allowing sufficient interspace by zero padding to include the end effect. Similar computational models are constructed in [70] and [71] on the MLU001 vehicle (RTRI), utilizing the 2D magnetic vector potential of the magnetic sources to increase the force accuracy relative to inductance modelling based on filament currents.

A simpler, lumped inductance model approach is pursued in [42] by researchers at Argonne National Laboratories in the U.S., and is used to evaluate the sidewall mounted, null-flux system for levitation, guidance and propulsion [72], which is a pre-runner to the present MLX series of vehicles at the Yamanashi test track in Japan (RTRI). The models neglects eddy current losses, and an overestimate of the L/D ratio of 250 at 500 km/h is calculated.

A modelling improvement over its predecessors, on the MLX series of vehicles, is [73],[37] reported by a joint collaboration between Tokyo and Kansai Universities and Mitsubishi. The articles incorporate eddy losses in the cryostat shielding plates, but omit heave velocity in the stiffness and damping models [36].

The late models provided by the LLNL team [26] using a PM source for levitation, contain approximation very similar to the "semi-quantitative calculations" in [28], and the brief article [25] has a promotional character. The General Atomics' Urban Maglev project has been reported in conference proceedings [74]-[76], besides the early journal paper [29] conveying a miniature rotating disk experiment.

We benefit from the collaboration with the General Atomics team, providing valuable experimental data from their second rotating wheel facility, and we have consulted with Post at LLNL on several occasions.

2 Our contribution

We contribute to the evolution of discrete track EDS by developing a model with infinitely many track loops labeled the Infinite Track Model (ITM). We thereby avoid the problem with finite current models of linear machinery, where the number of track current states limit the maximum timespan of the model. An infinite track is especially important for EDS maglev as the natural mechanical resonance has a very long wavelength relative to D/v^x (the track loop interspacing D scaled over propulsion velocity v^x), and a high number of track conductors must be incorporated to evaluate the stability of mechanical resonance. In addition, for densely spaced tracks, the mutual inductance between the track conductors is significant, and we derive methods to estimate the field coupling effect due to conductor stranding and changes in the track current density vector field pattern from eddy currents, skinning and the proximity effect.

We start our derivation from Maxwell's equations by developing a coupled PDE-ODE to conceptualize the effect of the moving source frame and to illuminate the modelling challenges. We explain the assumptions we make in simplifying this PDE model and distinguish between time-varying magnetic coupling caused by relative movement as opposed to a time-varying current density vector field pattern. We account for eddy currents in solid material using power loss and damping coefficients and state the limitations of this modelling.

We incorporate the 3D geometry of the magnetic source in contrast to the traditional inductance modelling, which typically assumes a flat or filament source current geometry. This allows for high magnetic field accuracy, reducing the force error which is proportional to the square of the magnetic field error.

The time-varying part of the mirror magnetic field in the track is in first approximation proportional to $(D/\lambda)^4$ (see Appendix C), where λ is the dominant wavelength of the source. This justifies our assumption of ignoring the magnetic flux from the induced currents in the source for densely spaced tracks despite a moderate clearance between the track and the source. These induced source currents are accounted for using power loss and damping coefficients[5].

Our approach also applies to SC maglev, where the same assumption is partly justified by the weak mirror

[5] This approximation is even better for NdFeB permanent magnet (PM) sources which have a high resistivity $144 \cdot 10^{-8}$ Ωm, two orders of magnitude larger than copper [77].

magnetic field in the track, high track-to-source clearance and shielding of the SC magnets. In addition, our models encompass all previous discrete track EDS models in a generalized framework. To our knowledge, we develop the first discrete track EDS models unifying both dynamics and statics. The ITM is amendable for harmonic analysis to compute static properties like lift and drag forces, and can be truncated to an ODE for precise and efficient numerical simulation of the dynamics.

2.1 Organization

Later in Section 3, we present notation and nomenclature. In Section 3, we derive a general coupled PDE-ODE governing all EDS maglev, and explain the challenge of simplifying this model with filament currents. We motivate essential concepts and state the underlying assumptions of our modelling in Section 4. We provide the peculiarities of litz wire and give criteria for the model reduction in Section 6, whereas in Section 5 the governing equations are derived. In Section 8, we provide a brief conclusion. Some calculations have been relegated to the Appendix.

2.2 Notation

The coordinate systems are oriented as in Figure 1, with the x-axis as the horizontal or *propulsion direction*; the y-axis is the vertical or *levitation direction*, while z is directed transverse to the propulsion and levitation direction in the *lateral* direction. We reserve superscripts for name labeling as $\mathbf{B}^s$ and i^{loop}, and use subscript for number indexing like i_n and i_{m+1}. In addition, lower subscripts x, y and z are used to denote scalar component functions $\mathbf{B} = (B_x, B_y, B_z)$, such that $B_x \triangleq \mathbf{B} \cdot \hat{\mathbf{e}}_x$, where '$\cdot$' is vector (inner) product in $\mathbb{R}^3$. For brevity, the dependence on the position vector $\mathbf{p}$ is occasionally omitted in vector fields, so that $\mathbf{B} \triangleq \mathbf{B}(\mathbf{p})$. Calligraphic $\mathcal{B}$ represent magnetic flux density integrated over the transverse direction as $\mathcal{B}(x, y) \triangleq \int_{-w/2}^{w/2} \mathbf{B}(x, y, z) dz$; moreover, when no ambiguity can arise, we refer to the magnetic flux density vector $\mathbf{B}$ as "the magnetic field", which is justified by the constant permeability $\mathbf{B} = \mu_0 \mathbf{H}$. The magnetic vector density $\mathbf{B}^i$ is created by the filament current i, whereas $\mathbf{B}^{\mathbf{J}}$ is caused by the current vector density $\mathbf{J}$. Curly braces are used to denote bi-infinite vectors $\{i_n\} \triangleq \{\ldots, i_{-2}, i_{-1}, [i_0], i_1, i_2, \ldots\} = i\{n\} = i\{n\}(t)$, where the square bracket identifies index number zero. The time argument is occasionally suppressed for brevity. The inner product between two such vectors is defined as $\langle \{a_n\}, \{b_n\} \rangle_n \triangleq \sum_{n=-\infty}^{\infty} a_n b_n$. The partial derivative is abbreviated $\partial_t \triangleq \partial/\partial t$ or $\partial_{xx} \triangleq \partial^2/\partial x \partial x$, and the Laplacian is denoted $\Delta \triangleq \partial_{xx} + \partial_{yy} + \partial_{zz}$. The boundary path (contour) of the $\mathbb{R}^3$ oriented surface P is denoted ∂P. We refer to Assumption 1 as (A1) and Condition 1 as (C1) etc.

The following abbreviations are used:
PDE - Partial Differential Equation
ODE - Ordinary Differential Equation
FEM - Finite Element Method
DOF - Degrees of Freedom
3D - Three dimensional
maglev - magnetic levitation
EDS - Electrodynamic Suspension
SC - Superconductor
PM - Permanent Magnet
ITM - Infinite Track Model
PTM - Periodic Track Model
LPM - Lumped Parameter Model

2.3 Nomenclature

Symbol	Interpretation
$\mathbf{p} \triangleq (x, y, z)$	Vector coordinates in the stationary frame
$'\mathbf{p} \triangleq ('x,' y,' z)$	Vector coordinates in the moving frame
$\nabla_{\mathbf{p}}$	Gradient with respect to the vector $\mathbf{p}$
$\mu(\mathbf{p}), \mu$	Material permeability at position $\mathbf{p}$
$\rho(\mathbf{p}), \rho$	Material resistivity at position $\mathbf{p}$
$\mathbf{B}^s$	Source magnetic field
$\mathbf{B}^J$	Magnetic field created by track currents $\mathbf{J}$
$\mathbf{B}^{tot} = \mathbf{B}^s + \mathbf{B}^J$	Total magnetic field
$\mathbf{J}$	Vector current density induced by $\mathbf{B}^s$
$\mathbf{J}_n^{loop}$	Vector current density in loop n
i_n^{loop}, i_n	Loop current n from rung $(n-1)$ to n
i_n^{rung}	Current in the n-th rung $i_n^{rung} = i_{n-1}^{loop} - i_n^{loop}$
$i\{n\}, \{i_n\}$	Bi-infinite loop current vector
P	Open surface of flux penetration
P_n	Surface for loop n
∂P	The boundary path (contour) of P
∂P_n^{ϕ}	Filament location for flux considerations for loop n
∂P_n^{F}	Filament location for force consideration for loop n
A	Cross-section area of a conductor
V	Volume of a current
$\mathbf{F}^{tot}$	Total force
F^d	Drag force
F^l	Lift force
$\mathbf{F} \triangleq (F^d, F^l, 0)$	Force between levitated object and the track
$\mathbf{F}^{in}$	Input force
$\mathbf{F}^{par}$	Force created by parasitic dissipation, see (68)
$\boldsymbol{\alpha}^{par}$	Parasitic dissipation (damping) $\boldsymbol{\alpha}^{par} \triangleq (\alpha_x^{par}, \alpha_y^{par}, 0)$, see (65)
$\boldsymbol{\alpha}^{m}$	Mechanical dissipation (damping) $\boldsymbol{\alpha}^{m} \triangleq (\alpha_x^{m}, \alpha_y^{m}, 0)$
y	Distance from lower edge of the source to the vertical center of a rung (vertical distance between the frames)
$y^F \triangleq y - \Delta y^F$	Effective force levitation height for producing correct force with filament approximation
Δy^F	Decrease in levitation height for force considerations for single-sided sources
$y^{Fl} \triangleq y - \Delta y^{Fl}$	Effective lift force levitation height for double-sided sources
$y^{Fd} \triangleq y - \Delta y^{Fd}$	Effective drag force levitation height for double-sided sources
$\Delta\phi$	Horizontal increase in the flux window contour P_n^{ϕ}
$v_x, v^x = d\mathbf{p}/dt \cdot \hat{\mathbf{e}}_x$	Propulsion velocity
δc	Diameter of a strand of litz wire
N	Number of strands in a litz wire
E_n	Electromotive force (e.m.f.) in loop n
$\{E_n\}$	Bi-infinite e.m.f. vector
D	Centerline distance between rungs
λ	Fundamental wavelength of $\mathbf{B}^s$
$\Gamma^x\{nD\}$	Sampling operator, see (29)
w	Lateral width of a track loop
L	Average self-inductance of a track loop
M_k	Average mutual inductance between loops k loops apart
$\{l_n\}$	Inductance vector
R_b	Average sidebar resistance
R_r	Average rung resistance
$\mathcal{L}$	Track inductance matrix, see (35)
$\mathcal{R}$	Track resistance matrix, see (36)

3 Model with vector current density

We start by deriving the model from Maxwell's equations, using vector current density $\mathbf{J}$ for a general track, to reveal the structure of the equations and to provide criteria to guide the approximation to filament currents. Thereafter, we proceed to handle the specific geometry of the track, like the ones shown in Figure 1, in terms of conductor orientation and stranding.

Electrodynamic suspension magnetic levitation of a rigid body is described by a PDE, governing the currents, coupled to an ODE determining the motion of the body. We call the PDE, derived from Maxwell's equations, the *current equation*, while the ODE, stemming from Lorentz forces between the track currents and the source magnetic field, is named the *mechanical equation*, and constitutes the rigid body dynamics of the vehicle.

3.1 Reference frames and derivatives in the inertial frame

The model has two coordinate frames. The *inertial frame* $(\hat{\mathbf{e}}_x, \hat{\mathbf{e}}_y, \hat{\mathbf{e}}_z)$ is fixed to the track at the geometrical center of a track rung, and coordinates resolved in this frame are denoted $\mathbf{p} = (x, y, z)$. The *moving frame* $('\hat{\mathbf{e}}_x, '\hat{\mathbf{e}}_y, '\hat{\mathbf{e}}_z)$ with coordinates $'\mathbf{p} = ('x, 'y, 'z)$ is attached to the lower edge of the moving source current as shown in Figure 1. If the moving frame is rotating with an angular velocity vector expressed in the inertial frame $\mathbf{\Omega} = (\Omega_x, \Omega_y, \Omega_z)$, the total derivative of a vector expressed in the inertial frame d/dt of a vector quantity attached to the moving frame, becomes after applying the chain rule and the transport theorem from mechanics [78], p. 114, [79], p. 121,

$$\frac{d}{dt} = \nabla_{\mathbf{p}} \cdot \frac{d\mathbf{p}}{dt} + \frac{'d}{dt} + \mathbf{\Omega}\times, \tag{1}$$

where $'d/dt$ is the time derivative in the moving frame, $\nabla_{\mathbf{p}}$ is the gradient operator with respect to the vector $\mathbf{p} = (x(t), y(t), z(t))$ expressing the moving frames origin resolved in the inertial frame. When this derivative is applied to the track current, $\nabla_{\mathbf{p}} \cdot d\mathbf{p}/dt$ and $\mathbf{\Omega}\times$ introduce the velocities $(dx/dt, dy/dt, dz/dt)$ and $(\Omega_x, \Omega_y, \Omega_z)$ respectively, into the current equation that are vital for the dynamics. Unfortunately, indiscriminately replacing $d\mathbf{p}/dt$ with $(v^x t, 0, 0)$ to represent rectilinear motion is common practice in the maglev community, but gives incorrect levitation dynamics as it ignores the dependency on heave velocity dy/dt. For brevity of presentation, we will set $\mathbf{\Omega} = 0$ in further derivations.

3.2 Track current equation

Maxwell's Equations under quasistatic conditions are defined by ignoring displacement current and assuming Ohm's Law, so that there is no free charge inside the conductors. The conditions are mainly justified by the field wavelengths being sufficiently longer than the spatial dimensions[6]. Let $\mathbf{B}$ denote the magnetic flux density; $\mathbf{H}$ and $\mathbf{E}$ are the magnetic and electric field intensity respectively, and $\mathbf{J}$ is the current density. The quasistatic equations are

$$\nabla \cdot \mathbf{B} = 0 \tag{2}$$

$$\nabla \times \mathbf{E} = -\frac{d}{dt}\mathbf{B} \tag{3}$$

$$\nabla \times \mathbf{H} = \mathbf{J} \tag{4}$$

$$\nabla \cdot \mathbf{J} = 0, \tag{5}$$

where Gauss Law for electric fields has been replaced with the continuity equation (5), which is a consequence of removing the displacement current $\partial_t \mathbf{D}$. We assume an isotropic medium, so that the constitutive relations are

$$\mathbf{B} = \mu(\mathbf{p})\mathbf{H}, \quad \mathbf{E} = \rho(\mathbf{p})\mathbf{J}, \tag{6}$$

and the last equation is Ohm's Law. The scalar functions $\mu(\mathbf{p})$, $\rho(\mathbf{p})$ are the permeability and resistivity of the material at position $\mathbf{p}$, respectively. Notice that the track geometry is implicit in (6). The boundary and

[6] See [80], Chap 7, for underlying physical prerequisites

interface conditions between two materials 1 and 2 are

$$(\mathbf{B}_1 - \mathbf{B}_2) \cdot \hat{\mathbf{n}}_{12} = 0 \quad (7)$$

$$(\mathbf{E}_1 - \mathbf{E}_2) \times \hat{\mathbf{n}}_{12} = 0 \quad (8)$$

$$(\mathbf{H}_1 - \mathbf{H}_2) \times \hat{\mathbf{n}}_{12} = \mathbf{K}, \quad (9)$$

where $\hat{\mathbf{n}}_{12}$ is the normal surface vector directed from material 1 into 2, and $\mathbf{K}$ is a surface current on the material interface.

We partition the total magnetic flux density at any point into $\mathbf{B}^{tot} = \mathbf{B}^s + \mathbf{B}^J$ where $\mathbf{B}^s$ is the *source magnetic field*, and $\mathbf{B}^J$ is the magnetic field from the track loops caused by the induced current $\mathbf{J}$. Taking the curl of (3), and substituting in (4) and (6), yields

$$\nabla \times \nabla \times \boldsymbol{\rho}(\mathbf{p})\mathbf{J} = -\mu(\mathbf{p})\frac{d}{dt}\mathbf{J} - \nabla \times \frac{d}{dt}\mathbf{B}^s. \quad (10)$$

Using the vector field identity $\nabla \times \nabla \times \mathbf{F} = \nabla(\nabla \cdot \mathbf{F}) - \Delta\mathbf{F}$, and expanding $d/dt\,\mathbf{B}^s$ in the stationary reference frame as in (1), gives the *track current equation*

$$\frac{d}{dt}\mathbf{J} = \rho(\mathbf{p})\mu^{-1}(\mathbf{p})\Delta\mathbf{J} - \mu^{-1}(\mathbf{p})\nabla \times \left({}'\partial_t\mathbf{B}^s + \nabla_{\mathbf{p}}\mathbf{B}^s \cdot \frac{d\mathbf{p}}{dt}\right), \quad (11)$$

where current continuity (5) is imposed. Here we have used that $\Delta(\rho(\mathbf{p})\mathbf{J}) = \rho(\mathbf{p})\Delta\mathbf{J}$ by assuming that the resistivity is constant inside the conductor which also implies that $\nabla(\nabla \cdot \boldsymbol{\rho}(\mathbf{p})\mathbf{J}) = 0$ from (5). Equation (11) is a 3D diffusion equation with a source created by the movement of the body $d\mathbf{p}/dt$, and the time varying source currents causing ${}'\partial_t\mathbf{B}^s$. From here on, for brevity, we assume constant source currents so that $\mathbf{B}^s({}'\mathbf{p})$ is not an explicit function of time.

3.3 Mechanical equation

The force exerted on the track $\mathbf{F}^{tot}$ from the interaction of $\mathbf{B}^s$ with the current $\mathbf{J}$ is determined by the Lorentz force equation integrated over the volume V^J of the current

$$\mathbf{F}^{tot} = \int_{V^J} \mathbf{J} \times \mathbf{B}^{tot} dV, \quad (12)$$

where $\mathbf{B}^{tot}$ includes the magnetic field from the track itself $\mathbf{B}^J$. However, the induced field $\mathbf{B}^J$ only produces internal forces in the track, and integrates to zero in the dynamic equations. After removing $\mathbf{B}^J$, we are left with the *force* $\mathbf{F}$ between the levitated object and the track current

$$\mathbf{F} = \int_{V^J} \mathbf{J} \times \mathbf{B}^s dV. \quad (13)$$

By using Newton's second Law for the motion of the levitated object, and adding an input (propulsion) force $\mathbf{F}^{in}$, the dynamic equation called the *mechanical equation* is obtained

$$\frac{d^2}{dt^2}\mathbf{p} = \frac{1}{m}\int_{V^J} \mathbf{J} \times \mathbf{B}^s dV + \mathbf{F}^{in}, \quad (14)$$

which together with the track current equation (11) describes the motion of the levitated object.

3.4 Why filament models?

The models from the last section require further simplification before we can use them in design and analysis. The main requirements of the model are to: **i**) predict static and dynamic behavior, **ii**) relate design parameters,

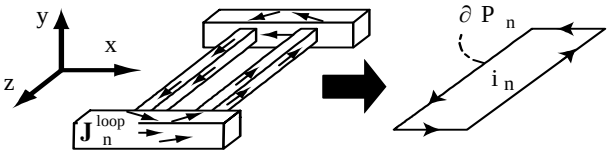

Figure 2: Challenge of filament modeling: Locate the contour ∂P_n so that the filament circuit (right) has properties matching those of the current density model (left).

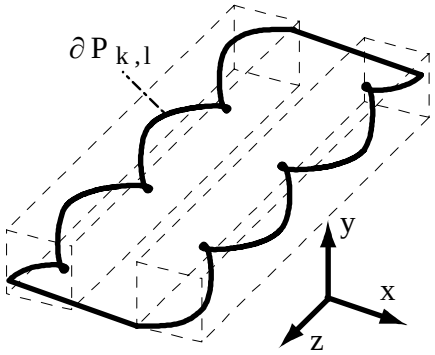

Figure 3: Contour $\partial P_{k,l}$ along the k-strand in the left rung and the l-strand in the right rung joined by the sidebars. Fine details of the litz wire have been omitted for clarity.

iii) provide accurate predictions and be computationally tractable. The model (11) and (14) is a coupled PDE-ODE. For each time step of the ODE, we must solve a 3D evolution equation with distributed source. Without approximations, devising algorithms based on Equation (11) and (14) is a formidable effort, and the resulting computational task is best suited for super computers. Moreover, such solutions convey few of the relationships between design parameters that guide a design.

By careful approximation, we aim to create simple models fulfilling the four requirements above.

3.5 Introduction to the filament approximation

This section addresses "filament modelling": The approach to replace the vector current density $\mathbf{J}_n^{loop}$ with a filament current i_n^{loop} for a track loop n, as shown in Figure 2. Unfortunately, a single filament location ∂P_n does not yield accurate approximations simultaneously for force, flux coupling, and inductance considerations.

Faraday's Law of induction (3), in integral form, for a track loop with current density $\mathbf{J}_n^{loop}$ yields

$$\oint_{\partial P_n} \rho \mathbf{J}_n^{loop} \cdot d\mathbf{l} = -\frac{d}{dt} \int_{P_n} \left(\mathbf{B}^s + \mathbf{B}^J \right) \cdot d\mathbf{S}, \tag{15}$$

where we have substituted $\mathbf{E}_n^{loop} = \rho \mathbf{J}_n^{loop}$ from (6), and the closed path of integration for the n-th loop ∂P_n is along an arbitrary loop strand $\partial P_{k,l}$ in Figure 3, while P_n is a corresponding (open) surface[7]. In this manner, there is ambiguity in the choice of ∂P_n which must be removed. We introduce the *loop current*

$$i_n^{loop} \triangleq \int_{A_n} \mathbf{J}_n^{loop} \cdot d\mathbf{S}, \tag{16}$$

[7] We are now using Stokes' theorem, which is valid for any simply connected (the path does not cross itself), closed path ∂P in $\mathbb{R}^3$.

where the area of integration A_n is taken over a cross-section of the whole n-th conductor [8], and the *loop resistance* is $R^{loop} = \oint_{\partial P_n} \rho \mathbf{J}^{loop} \cdot d\mathbf{l} \,/\, i_n^{loop}$ where again there is ambiguity in the choice of ∂P_n. After substitution, the left-hand-side of (15) becomes $R^{loop} i_n^{loop}$.

The flux coupling between track loops can be modelled with inductances under conditions that remains to be specified as

$$-\frac{d}{dt}\int_P \mathbf{B}^J \cdot d\mathbf{S} = -\sum_m l_m \frac{d}{dt} i_{n+m}^{loop}. \tag{17}$$

Here, l_m is the inductance between loop number zero and loop number m, whereas i_{n+m}^{loop} is the current in loop number $n+m$ as shown in Figure 4. Faraday's Law of induction for the n-th filament loop is now

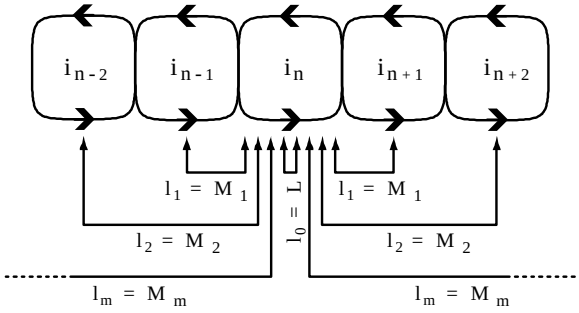

Figure 4: Schematic of the inductance coupling between track loops. Notice, that by superposition (from linearity of the medium), M_m is computed as if i_{n+m-1} and i_{n-m+1} are zero, even if i_m share a common rung with both i_{n+m-1} and i_{n-m+1}. Thus, separated loops and interconnected loops are treated similarly.

$$R^{loop} i_n^{loop} = -\frac{d}{dt}\int_{P_n^\phi} \mathbf{B}^s \cdot d\mathbf{S} - \sum_m l_m \frac{d}{dt} i_{n+m}^{loop}. \tag{18}$$

We have left to specify: the interpretation of the loop e.m.f. $R^{loop} i_n^{loop}$, the location and shape of the surface P_n^ϕ for flux integration, and the conditions under which the inductance modelling is valid.

Using the Lorentz force equation (13), we relate the force from $\mathbf{J}_n^{loop}$

$$\mathbf{F}_n^J = \int_{V_n^{loop}} \mathbf{J}_n^{loop} \times \mathbf{B}^s dV \tag{19}$$

to the force from the filament loop current i_n^{loop} in (16) along the contour ∂P_n^F as

$$\mathbf{F}_n^i = \int_{\partial P_n^F} i_n^{loop} d\mathbf{l} \times \mathbf{B}^s, \tag{20}$$

where the location of the contour ∂P_n^F is left to be decided.

4 Assumptions and setting

Our aim is to derive a dynamic equation in the time domain in the general form

$$\frac{dx}{dt} = f(x,t) \tag{21}$$

[8] To avoid ambiguity between loop i_n^{loop} and rung $i_n^{rung} \triangleq i_{n-1}^{loop} - i_n^{loop}$ currents, select the cross-section A_n at the sidebar.

labeled the *Infinite Track Model* (ITM), replacing the current equation (11) and the mechanical equation (14). This is done for a *bi-infinite* track (extending to infinity in both directions) to simplify later analysis and to avoid making unnecessary restrictive assumptions as pointed out in Section 2. We choose to model the *ladder track* shown in Figure 1 since this track has conduction coupling between the loops, which complicates the modelling compared to other discrete track topologies. In this sense, the ladder track is the most general. Separated discrete loops, without conduction coupling, is a simplification of this.

We aim to create models useful for design with parameters determined directly from physical properties without coefficients relying on judgement. It is also beneficial for designers to have models that do not depend on resource demanding measurements that are difficult to obtain in a typical maglev test environment with strong magnetic fields, high currents and small clearances. We attempt to meet this requirement.

We do not intend to describe the full 6DOF dynamics of a maglev vehicle, as the levitation system has to be supplemented with a guidance system of any flux type yielding a multitude of possible system arrangements. Instead, we constrain the motion to *2DOF* along the propulsion direction x and the levitation direction y, so that the lateral direction z is fixed. This setting increases the clarity of the presentation. However, our modelling approach can, with some modifications, be applied to combined levitation and guidance systems with 6DOF, and our methods provide a general framework for all discrete tracks geometries including: single loop-, double loop-, null-flux-, or ladder tracks composed of *stranded* (litz wire) or *solid conductors* with *linear conducting material*.

We assume a *spatial periodic geometry* in the propulsion direction, so the track resistance R^{loop} and the inductance vector $\{l_n\}_{n=-\infty}^{\infty}$ in (18) are the *statistical averages* over the track. This makes the track *shift-invariant* with respect to track loop number n.

Since maglev dynamics have modes close to the imaginary axis that are easily perturbed across this axis under approximations, we strive to maintain precision in, not only static, but also in dynamic currents and forces of the ITM. However, since we ignore lateral movement, the forces from the sidebars do not affect the dynamic equation, and are caused by $\mathbf{B}_z^s$ only as the forces from $\mathbf{B}_y^s$ cancels by symmetry. The $\mathbf{B}_z^s$ component is very small at the sidebars relative to $\mathbf{B}_x^s$ and $\mathbf{B}_y^s$ over the rungs for realistic source and track geometries. In addition, for densely spaced track D/w is small reducing the force contribution from the sidebars further to less than 1%, typically, of the total lift force as our research indicate. We have therefore chosen to ignore the sidebar force in further derivations[9].

We include a *mechanical dissipation* (damping) coefficient $\boldsymbol{\alpha}^m \triangleq (\alpha_x^m, \alpha_y^m, 0)$ contributing the force $d\mathbf{p}/dt \cdot \boldsymbol{\alpha}^m$ in the mechanical equation of the ITM to account for aerodynamic and mechanical damping. This term is not included in the vector current density model (14), but is vital for validation of experimental dynamics as a small aerodynamic damping contribution can be sufficient to stabilize the dynamics as Moon points out in [33], Chapter 5.

4.1 Changing current pattern and parameter dependence

Define the *current vector field pattern* in a track loop $\tilde{\mathbf{J}}_n^{loop}$, with the aid of i_n^{loop} in (16), as $\mathbf{J}_n^{loop} \triangleq i_n^{loop} \tilde{\mathbf{J}}_n^{loop}$, so that $\tilde{\mathbf{J}}_n^{loop}$ captures the geometry of the current flow. A requirement for using constant inductance and resistance, as in Section 3.5, is that $\tilde{\mathbf{J}}_n^{loop}$ is independent of the magnitude of the loop current i_n^{loop}. This is seen from the inductance between two arbitrary current elements $\mathbf{J}_m = i_m \tilde{\mathbf{J}}_m$ and $\mathbf{J}_n = i_n \tilde{\mathbf{J}}_n$, occupying volumes V_m and V_n respectively. The inductance is derived from the magnetic energy E_{mn}^J that under quasistatic conditions (see

[9] This is not to say that lateral dynamics are unimportant. For the Inductrack levitation system shown in Figure 1 without additional guidance force, the lateral dynamics has a low negative stiffness as RTRI anlysis indicate [81]. This has been experimentally confirmed by General Atomics [32].

Appendix A.1) become

$$E^J_{mn} = \frac{1}{2} M_{mn}\, i_m i_n = \frac{1}{2} \int\limits_{V_n} \mathbf{A}_m \cdot \mathbf{J}_n dV \tag{22}$$

$$= \frac{1}{4\pi} \iint\limits_{V_n} \int\limits_{V_m} \mu(\mathbf{p}_0) \frac{\mathbf{J}_m(\mathbf{p}_0) \cdot \mathbf{J}_n(\mathbf{p})}{|\mathbf{p} - \mathbf{p}_0|} dV(\mathbf{p}_0) dV(\mathbf{p}) \tag{23}$$

$$= \frac{1}{2} \left(\frac{1}{2\pi} \iint\limits_{V_n} \int\limits_{V_m} \mu(\mathbf{p}_0) \frac{\tilde{\mathbf{J}}_m(\mathbf{p}_0) \cdot \tilde{\mathbf{J}}_n(\mathbf{p})}{|\mathbf{p} - \mathbf{p}_0|} dV(\mathbf{p}_0) dV(\mathbf{p}) \right) i_m i_n, \tag{24}$$

where the term in the braces is the inductance M_{mn}, which is only constant if $\tilde{\mathbf{J}}_m$ and $\tilde{\mathbf{J}}_n$ are constant and independent of i_m and i_n. We refer to this condition as *stationary current vector field pattern*.

Due to eddy currents, skinning and proximity effects which vary with the excitation frequency, it is customary to assume that $R^{loop}(\omega)$ and $\{l_n(\omega)\}_{n=-\infty}^{\infty}$ vary with the current frequency ω. However, since the current is not monochromatic due to the end effect, including frequency dependency in the time domain equation (21) creates a non-causal system[10]. Instead, since the excitation frequency ω depends on the source field velocity relative to the track $|d\mathbf{p}/dt| = \sqrt{(v^x)^2 + (v^y)^2 + (v^z)^2}$, we parameterize the track parameters on the propulsion velocity v^x as $R^{loop}(v^x)$ and $\{l_n(v^x)\}_{n=-\infty}^{\infty}$, which accounts for skinning and proximity effect due to the propulsion velocity only. In static analysis, where v^x and the levitation height y are constant, we incorporate the full bandwidth characterisitics as $R^{loop}(\omega)$ and $\{l_n(\omega)\}_{n=-\infty}^{\infty}$. This increases the accuracy of the end effect that contributes the rise and decay of the currents which experience a different impedance than the dominant exitation frequency. With this convention in mind, we suppress the v^x or ω dependence in further notation.

The loss from eddy currents inside conductors and in surrounding conducting material are labeled *parasitic dissipation* and are accounted for by the parasitic damping coefficient $\boldsymbol{\alpha}^{par} \triangleq (\alpha_x^{par}, \alpha_y^{par}, 0)$ in the dissipative force $d\mathbf{p}/dt \cdot \boldsymbol{\alpha}^{par}$ in the mechanical equation. Here, α_x^{par} accounts for the parasitic resistive losses caused by propulsion velocity v^x, and losses created by levitation velocity v^y are captured via α_y^{par}. The underlying assumptions of this modelling are investigated in Section 7.1, and require the magnetic field from the parasitic currents to be small relative to the source field. Too much solid conductor material will therefore reduce the accuracy of the model.

4.2 Representation of the source magnetic field

For maglev applications, it is necessary to distinguish between inductance variations attributable to alterations in the current vector field pattern $\tilde{\mathbf{J}}$, and the variations in inductance caused by relative movement between stationary current vector field patterns. The flux coupling into the track from the source $\int_{P_n^\phi} \mathbf{B}^s \cdot d\mathbf{S}$ in (18) is oftentimes simply modelled as time-varying inductance $M(t)$. However, this yields incorrect dynamics unless the inductance is an explicit function of the position $\mathbf{p}$ and $d\mathbf{p}/dt$ as $M(\mathbf{p}, d\mathbf{p}/dt, t)$ [36]. Furthermore, since only the relative position between the source field $\mathbf{B}^s$ and the flux cutting surface P_n^ϕ is changing, we model the flux coupling into a track loop as $\phi_n(\mathbf{p}, d\mathbf{p}/dt) = \int_{P_n^\phi(\mathbf{p}, d\mathbf{p}/dt)} \mathbf{B}^s \cdot d\mathbf{S}$. This has the benefit of allowing for the precise geometry of the source current in $\mathbf{B}^s$ which is required for high force accuracy, but relies on conductor stranding to reduce the proximity effect which alters the current vector field pattern as a function of relative position $\mathbf{p}$.

The time varying part of the mirror magnetic field in the track in the moving reference frame is in first approximation proportional to $(D/\lambda)^4$ (see Appendix C). This justifies our assumption of ignoring the magnetic flux from the induced currents in the source for densely spaced tracks. This assumption is even better for NdFeB PM sources which have a high resistivity ($144 \cdot 10^{-8}$ Ωm, two orders of magnitude larger than copper [77]). These parasitic loss currents are accounted for in Section 7, and we therefore assume that the source magnetic field $\mathbf{B}^s(\mathbf{p})$ is independent of the track currents $\mathbf{J}$. Thus, *nonlinear source material is acceptable*, and will not make the current equation for discrete tracks, analogous to (11), nonlinear.

[10] The present value of a non-causal system depends on future values of the system.

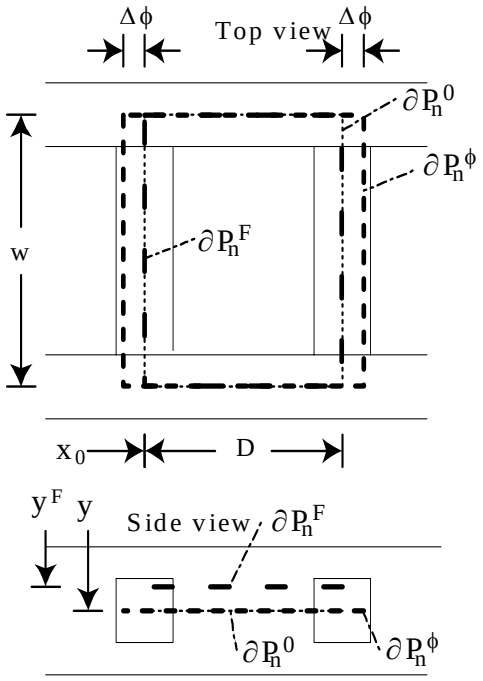

Figure 5: The choices of the filament path ∂P_n approximating loop n. ∂P_n^0 - contour along the center of the conductor, ∂P_n^ϕ - contour to match source flux, ∂P_n^F - contour to match force.

4.3 Flux cutting surface P_n^ϕ

The surface P_n^ϕ in the filament approximation (18) must be specified. Since the e.m.f. $R^{loop} i_n^{loop}$ and the resistance R^{loop} depends on the arbitrarily chosen contour ∂P_n^ϕ, we use an average over all paths $\partial P_{k,l}$ along the strands of the wire shown in Figure 3 to avoid ambiguity. The filament loop e.m.f. is defined as

$$R^{loop} i_n^{loop} \triangleq \frac{1}{N^2} \sum_{k=1}^{N} \sum_{l=1}^{N} \oint_{\partial P_{k,l}} \rho \mathbf{J}_n^{loop} \cdot d\mathbf{l}, \tag{25}$$

when excited by the source field $\mathbf{B}^s$.

4.4 Resolving the filament approximation

The ambiguities arising from the filament approximations and the track inductance modelling in Section 3.5 are resolved in Section 6. The surfaces P_n^ϕ and P_n^F are defined as in Figure 5. To account for the increased flux linkage of litz wire compared to filament loops (explained in Section 6), *the horizontal increase in the flux window* $\Delta\phi$ is introduced in P_n^ϕ.

The filament loop for force determination ∂P_n^F is located above the loop ∂P_n^0 at *the effective force levitation height* $y^F \triangleq y - \Delta y^F$, where Δy^F is the decrease in levitation height for force computations. For double-sided sources, this definition is refined, since the the lift and the drag forces must be computed from different filament loop locations as explained in Appendix B.2. Thus, y^{Fl} is *the effective lift force levitation height*, and y^{Fd} is *the effective drag force levitation height* for double-sided sources as indicated in Figure 6.

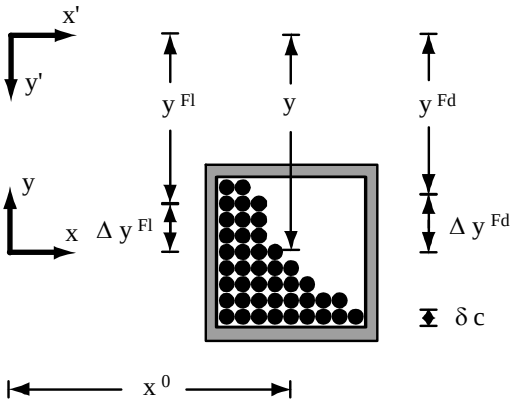

Figure 6: Schematic of a cross-section of a litz wire rung with casing. The body fixed coordinate system (x', y') is located at the lower edge of the magnetic source. For single-sided sources $y^F = y^{Fl} = y^{Fd}$.

5 Infinite Track Model with filament currents

We start by deriving a track current equation with filament loop currents i_n analogous to (11) for continuous tracks.

5.1 Track current equation for the ITM

Faraday's Law is used to derive the induced electromotive force for loop n denoted E_n using the contour ∂P_n^ϕ. As P_n^ϕ is normal to the y-axis, it cuts flux lines of the time-invariant source $\mathbf{B}^s$ as

$$E_n = -\frac{d}{dt}\int_{P_n^\phi} \mathcal{B}_y^s dx', \tag{26}$$

which is a function of the source's position $(x(t), y(t))$ resolved in the inertial frame. The horizontal position of

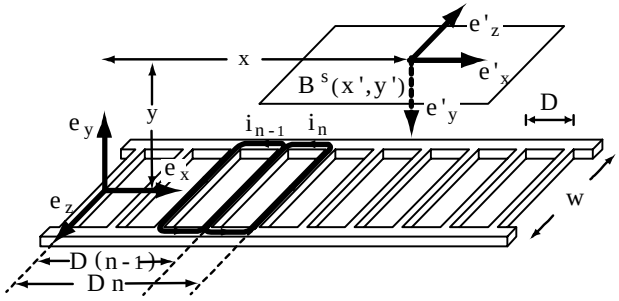

Figure 7: Schematic of the stationary frame (x, y, z) and the body fixed (moving) frame (x', y', z').

the n-th loop in the moving frame $x'(t)$, resolved in the stationary frame, becomes $x'(t) = Dn - x(t)$, as shown in Figure 7, and the horizontal distance between the frames is the same resolved in either's frames coordinates,

so that $y'(t) = y(t)$, and (26) becomes

$$E_n(x,y) = \frac{d}{dt}\Phi_n(x(t),y(t)) = \frac{d}{dt}\int\limits_{D(n-1)-x(t)-\Delta\phi(y)}^{Dn-x(t)+\Delta\phi(y)} \mathcal{B}_y^s(x',y)\,dx', \tag{27}$$

where we have used that $\hat{\mathbf{e}}_y = -\hat{\mathbf{e}}'_y$. The derivative in (27) is evaluated using Leibnitz's rule

$$E_n(x,y) = -\left.\mathcal{B}_y^s(x',y(t))\right|_{D(n-1)-x(t)-\Delta\phi(y)}^{x'=Dn-x(t)+\Delta\phi(y)} \frac{dx}{dt} \quad + \int\limits_{D(n-1)-x(t)-\Delta\phi(y)}^{Dn-x(t)+\Delta\phi(y)} \partial_y\,\mathcal{B}_y^s(x',y)\,dx'\,\frac{dy}{dt}. \tag{28}$$

Here, we utilized the assumption that $\partial_y\Delta\phi(v^x,y) = 0$ which is justified in Section 6.6.

At this point, some notation needs to be introduced. Since the track is periodic or shift-invariant in the x-direction, we introduce the *sampling operator* $\Gamma^x\{nD\}$, taking an infinite number of translated samples in the x-direction with lattice constant D, as

$$\Gamma^x\{nD\}f(x,y) \triangleq \{\ldots, f(-D-x',y), [f(-x',y)], f(D-x',y),\ldots\} \;\Big|\; \begin{matrix} x'=x(t) \\ x'=x(t)-D \end{matrix}. \tag{29}$$

Similarly, we define

$$\Gamma^x_{\Delta\phi}\{nD\}f(x,y) \triangleq \{\ldots, f(-D-x',y), [f(-x',y)], f(D-x',y),\ldots\} \;\Big|\; \begin{matrix} x'=x(t)-\Delta\phi(y) \\ x'=x(t)-D+\Delta\phi(y) \end{matrix}, \tag{30}$$

to incorporate the increase in the flux window from the parameter $\Delta\phi$. Using this notation, we define the bi-infinite e.m.f. vector $\{E_n(x,y)\} \triangleq \{\ldots, E_{-1}(x,y), [E_0(x,y)], E_1(x,y),\ldots\}$ from (28) as

$$\{E_n(x,y)\} = -\Gamma^x_{\Delta\phi}\{nD\}\mathcal{B}_y^s(x,y)\,\frac{dx}{dt} \quad + \quad \Gamma^x_{\Delta\phi}\{nD\}\int\limits_{P^\phi} \partial_y\,\mathcal{B}_y^s(x',y)\,dx'\,\frac{dy}{dt}, \tag{31}$$

and will use it in the next section to derive the track current equation.

5.1.1 Inductance matrices and operators

In this section, we generalize the single loop in Figure 2 to a *bi-infinite* track along the x-axis as shown in Figure 7.

We define the track current vector $i\{n\}$, by ordering the loop currents as

$$\{i_n\} \triangleq \{\ldots, i_{-2}, i_{-1}, [i_0], i_1, i_2, \ldots\} = i\{n\}, \tag{32}$$

where we henceforth use $i_n = i_n^{loop}$. From the assumed *statistical averaged track geometry*, the electrical properties of each track loop are identical to all other loops; the track is *shift invariant* (with respect to loop number n), and the bi-infinite *inductance vector* $\{l_n\}$ (see Figure 4) also becomes shift invariant

$$\{l_n\} \triangleq \{\ldots, M_2, M_1, [L], M_1, M_2, \ldots\}, \tag{33}$$

where L is the loop self inductance, and M_m is the mutual inductance between two loops separated by $m-1$ loops (see Sections 6.3). We now write the e.m.f. from track coupling in (18) as an inner product $\langle\{l_m\}, d/dt\,\{i_{n+m}\}\rangle_m = \sum_m l_m d/dt\, i_{n+m}$. Notice, this description is appropriate with, or without, conduction coupling between the loops, as explained in Figure 4.

We now generalize (18) from a single loop to a track, using the e.m.f. vector (31), arriving at the vector equation indexed by loop number n as

$$\left\{\sum_m l_{n-m}\frac{d}{dt}i_m\right\} = -\left\{R^{loop}i_n\right\} - \{E_n(x,y)\}. \tag{34}$$

The convolution sum $\{\sum_m l_{n-m} d/dt\, i_m\} = \mathcal{L} d/dt\, i\{n\}$ is rewritten using an infinite dimensional inductance matrix $\mathcal{L}$, where each row increment is the inductance vector (33) shifted one entry to the right, as

$$\mathcal{L} \triangleq \begin{bmatrix} \ddots & \vdots & \vdots & \vdots & \\ \cdots & L & M_1 & M_2 & \cdots \\ \cdots & M_1 & [L] & M_1 & \cdots \\ \cdots & M_2 & M_1 & L & \cdots \\ & \vdots & \vdots & \vdots & \ddots \end{bmatrix}. \tag{35}$$

A matrix constructed from one vector in this manner is called *circulant symmetric*, or a (discrete) *convolution operator*.

The resistance vector, unlike the inductance vector, depends on the conductor coupling. In the case of no conductor coupling, $\left\{R^{loop} i_n\right\} = R^{loop} i\{n\}$. With conductor coupling, we introduce R_r as the *rung resistance*, and R_b as the *sidebar resistances* as shown in Figure 8. A mesh analysis of this track gives $\left\{R^{loop} i_n\right\} = \mathcal{R} i\{n\}$,

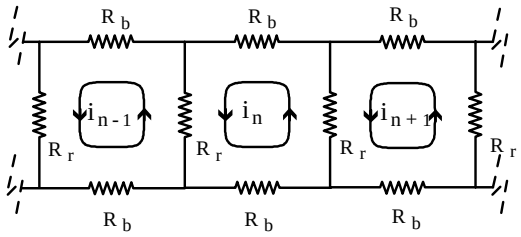

Figure 8: Schematic of the resistance to the ladder track.

where the infinite dimensional resistance matrix $\mathcal{R}$ is

$$\mathcal{R} \triangleq \begin{bmatrix} \ddots & \vdots & \vdots & \vdots & \cdots \\ \cdots & 2(R_r + R_b) & -R_r & 0 & \cdots \\ \cdots & -R_r & [2(R_r + R_b)] & -R_r & \cdots \\ \cdots & 0 & -R_r & 2(R_r + R_b) & \cdots \\ & \vdots & \vdots & \vdots & \ddots \end{bmatrix}. \tag{36}$$

The total magnetic energy of the track is $\sum_n \sum_m l_{n-m} i_n i_m = \langle i\{n\}, \mathcal{L} i\{n\} \rangle_n > 0$ for $i\{n\} \neq 0$. From this, we infer that the inductance matrix is positive definite, and the inverse matrix $\mathcal{L}^{-1}$ is well-defined, so that Faraday's Law (34) can be rewritten

$$\frac{d}{dt} i\{n\} = -\mathcal{R}\mathcal{L}^{-1} i\{n\} - \mathcal{L}^{-1}\{E_n(x,y)\}, \tag{37}$$

where we have used that $\mathcal{R}$ and $\mathcal{L}^{-1}$ commute since they are both convolution operators, and convolution is commutative [82]. Equation (37) is the *track current equation* for a filament track, analogous to (11). This is to our knowledge, the first formulation to capture mutual inductance without track truncation.

5.2 Mechanical equation for the ITM

We derive the mechanical equation for the track in Figure 7 analogous to (14) for continuous tracks. We consider 2DOF horizontal and vertical linear motion of a rigid body. By adding lateral dynamics and Euler's equation for rotational motion, the dynamics can be extended to 6DOF.

5.2.1 Force from a rung

The force between the right rung in loop number n and the magnetic field $\mathbf{B}^s$, as shown in Figure 7, is

$$\mathbf{F}_n(y^F) = \int_{-w/2}^{w/2} (i_{n+1} - i_n)\hat{\mathbf{e}}_z \times \mathbf{B}^s dz = (i_{n+1} - i_n)\hat{\mathbf{e}}_z \times \mathcal{B}^s(x', y^F), \tag{38}$$

where $\mathbf{F}_n$ is zero in the $\hat{\mathbf{e}}_z$ direction. Resolving x' in the stationary reference frame for loop n as $x' = Dn - x$, and using the fact that $y^F = y'^F$, the magnetic field at rung n's position is $\mathcal{B}(Dn - x, y^F)$. The total force, exerted between the track and the levitated object, $\mathbf{F}^a = \sum_{n=-\infty}^{\infty} \mathbf{F}_n^a$, becomes

$$\mathbf{F}(y^F) = \sum_{n=-\infty}^{\infty} \left[\hat{\mathbf{e}}_z \times \mathcal{B}^s(D(n-1) - x, y^F) - \hat{\mathbf{e}}_z \times \mathcal{B}^s(Dn - x, y^F)\right] i_n. \tag{39}$$

Since (39) is a telescopic series, the infinite sum is rewritten as an inner product over all track currents $i\{n\}$, using the track sampling operator $\Gamma^x\{nD\}$ (29), as

$$\mathbf{F} = -\hat{\mathbf{e}}_z \times \left\langle \Gamma^x\{nD\}\, \mathcal{B}^s(x, y^F), i\{n\} \right\rangle_n. \tag{40}$$

The $\hat{\mathbf{e}}_x$ component of the magnetic field $\mathcal{B}_x^s$ gives rise to a *levitation force* F^l acting in the $y-$direction, and $\mathcal{B}_y^s$ creates a magnetic *drag force* F^d in the x-direction.

5.2.2 Force dynamics

From the definition of the effective force levitation height y^F in Section 4.4, we deduce that $dy_F/dt = dy/dt$, and $d^2y^F/dt^2 = d^2y/dt^2$. Including the *parasitic damping coefficient* $\boldsymbol{\alpha}^{par} = (\alpha_x^{par}, \alpha_y^{par}, 0)$ (discussed in Section 7) and the vertical part of the mechanical damping $\boldsymbol{\alpha}^{par} = (\alpha_x^m, \alpha_y^m, 0)$ in addition to the *propulsion force* $\mathbf{F}^{in} = (F_x^{in}, F_y^{in}, 0)$, Newton's second Law for the levitation dynamics become

$$m\frac{d^2y}{dt^2} = F_y^{in} + F^l - \alpha_y^{par}\frac{dy}{dt} - \alpha_y^m\frac{dy}{dt} - mg, \tag{41}$$

where g is the acceleration of gravity, and m is the mass of the levitated object.

Similarly, introducing the parasitic drag force $\alpha_x^{par}dx/dt$ and the horizontal mechanical damping force $\alpha_x^m dx/dt$, the force balance along the propulsion direction is

$$m\frac{d^2x}{dt^2} = F_x^{in} - F^d - (\alpha_x^{par} + \alpha_x^m)\frac{dx}{dt}. \tag{42}$$

With the exception of the mechanical damping term $\alpha_x^m dx/dt$, (41) and (42) are analogous to (14) with the current vector density $\mathbf{J}$.

5.3 Governing equations

Taking the track current equation (37), and substituting in the bi-infinite e.m.f. vector (31), yields the *track current equation for filament currents* (43) below, which is analogous to (11) for vector current density $\mathbf{J}$. Substituting the lift and drag force from (40) into the dynamic equations, (41) and (42), gives the *mechanical equation for filament currents* (45) and (44). The governing equations for the Infinite Track Model (ITM) are

$$\frac{d}{dt}i\{n\}(t) = -\mathcal{L}^{-1}\mathcal{R}i\{n\}(t) + \mathcal{L}^{-1}\Gamma_{\Delta\phi}^x\{nD\}\,\mathcal{B}_y^s(x,y)\frac{dx}{dt} - \mathcal{L}^{-1}\Gamma_{\Delta\phi}^x\{nD\}\int_{P^\phi}\frac{\partial}{\partial y}\mathcal{B}_y^s(x',y)\,dx'\,\frac{dy}{dt} \tag{43}$$

$$\frac{d^2x}{dt^2} = \frac{1}{m}\left\langle \Gamma^x\{nD\}\,\mathcal{B}_y^s(x, y^{Fd}), i\{n\}(t)\right\rangle_n - \frac{1}{m}(\alpha_x^{par} + \alpha_x^m)\frac{dx}{dt} + \frac{1}{m}F_x^{in} \tag{44}$$

$$\frac{d^2y}{dt^2} = -\frac{1}{m}\left\langle \Gamma^x\{nD\}\,\mathcal{B}_x^s(x, y^{Fl}), i\{n\}(t)\right\rangle_n - \frac{1}{m}\left(\alpha_y^{par} + \alpha_y^m\right)\frac{dy}{dt} + \frac{1}{m}F_y^{in} - g. \tag{45}$$

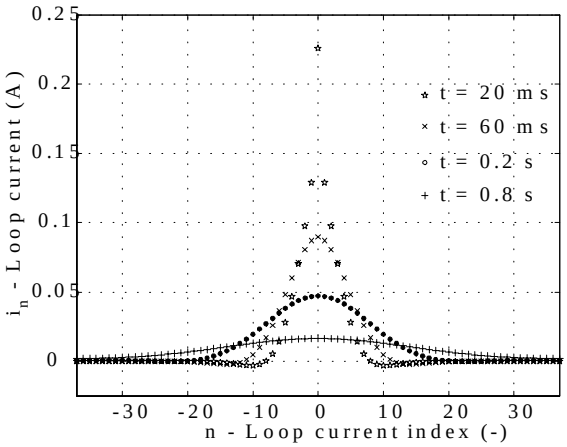

Figure 9: Green's function for the track operator $d/dt + \mathcal{L}^{-1}\mathcal{R}$. Equivalently, the response of $d/dt\, i\{n\}(t) = -\mathcal{L}^{-1}\mathcal{R} i\{n\}(t)$ to a unit impulse initial condition $i\{n\}(0) = \delta\{0\}$. Parameter values are taken from the General Atomics' test-wheel facility.

The track current equation (43) is discretized diffusion on a line with a source, and has the same structure as (11), where $\mu^{-1}(\mathbf{p})\Delta\mathbf{J}$ is replaced by $-\mathcal{L}^{-1} i\{n\}(t)$, and $\boldsymbol{\rho}(\mathbf{p})$ with $\mathcal{R}$. The Green's function $G\{n\}(t)$ for the $d/dt + \mathcal{L}^{-1}\mathcal{R}$ operator, or differently stated, the response of $d/dt\, i\{n,t\} = -\mathcal{L}^{-1}\mathcal{R} i\{n\}(t)$ to an impulse initial condition $i\{n\}(t_0) = \delta\{0\}$, is shown in Figure 9, and reveals the diffusion of the track currents.

6 Filament Approximation

Here we continue the issue of approximating the current vector density $\mathbf{J}_n^{loop}$ with a filament current i_n^{loop} for flux, force and inductance considerations, as initiated in Section 3.5. But first, we need to address the challenges posed by litz wire.

6.1 Litz wire properties

A *litz wire* is a bundled cable with insulated strands woven in a systematic pattern. Stranding the conductor increases the current carrying cross-section area (especially at higher frequencies), reduces eddy currents from flux gradients over the conductor, and consequently the ohmic losses $\int \rho |\mathbf{J}|^2 dV$. The weaving pattern equalizes proximity effects, maximizing the current carrying cross-section area, and evens out the currents between different strands. The length along the cable in which the weaving pattern repeats itself is called one *transposition*.

Traditionally, litz wire is used in transformers and inductors to reduce ohmic losses and to improve the quality-factor of the circuits. We repeat the definition of litz wire given in [83]:

Definition 1 ***An ideal litz wire***
Individual wires of the strand are enamelled and weaved along the entire divided conductor in such a way that all wires successively pass through all points of the cross-section.

For litz wire, it is customary to assume the following as in [84],[83],[85],[86]:

Assumption 1 ***Current equalization***
Each strand in the litz wire carries the same current i/N, where N is the number of strands in the litz wire.

However, the degree to which current equalization is achieved depends on the quality of the litz wire weaving pattern, the inducing field, and the circuit geometry. We state explicitly two conditions normally assumed for current equalization:

Condition 1 ***Long longitudinal wavelength of the source field***
The source field changes slowly along the length of the litz wire compared to the length of one transposition.

Condition 2 ***Large free air to conductor flux ratio***
The flux through free air (or core material) enclosed by the circuit is large compared to the source flux penetrating the litz wire.

Both conditions are typically satisfied in transformers and inductors and enable defining their ac-resistance [84],[83],[85],[86]. Therefore, little attention is paid to (C1) and (C2) in the design of these magnetic components.

For maglev applications however, (C1) and (C2) are rarely satisfied. For the ladder track in Figure 3, the litz wire rungs are closely spaced, with only a couple of transpositions per rung. In addition, the source flux density is concentrated at the lateral center of each rung and the slope of the decay is steep to either side. The consequences of this is violation of (A1), and the litz wire loop in Figure 3 picks up some of the flux in the $x-$ and $z-$direction. To demonstrate this effect, we make the mild technical assumption as in [83]:

Assumption 2 ***Spatial smoothing of the magnetic field***
The magnetic source $\mathbf{B}^s$ *is assumed constant over the cross-section of a strand.*

This is a very good assumption, since the high frequency components quickly decay away from the source. The quality of (A2) increases with the number of strands and is not restrictive for maglev applications.

We define the loop current for two side-by-side rungs (shown in Figure 3) as the sum of all combination of strand current loops $i_{k,l}^{strand}$ through strand k in the left rung and through strand l in the right rung as

$$i^{loop} = \frac{1}{N}\sum_{k=1}^{N}\sum_{l=1}^{N} i_{k,l}^{strand}. \tag{46}$$

From the generalized form of Stoke's theorem as in (15), the flux trough the loop carrying the current $i_{k,l}^{strand}$ is determined solely by the boundary of the surface $P_{k,l}$ that goes through strands k and l and the sidebars. Notice that the path $\partial P_{k,l}$ on the boundary of the surface $P_{k,l}$ is not contained in any hyperplane.

It is evident that flux through $P_{k,l}$ depends on the vertical flux B_y^s, the horizontal flux B_x^s, and the lateral flux B_z^s. However, since the source field $\mathbf{B}^s$ decays with a steep slope to either side transversely, relative to the transposition of the litz wire, the B_x^s and B_z^s flux does not necessarily cancel out in the sum (46) with the net result that the litz wire experience more flux than a filament loop ∂P^0 located in the center of the loop conductors. We refer to this effect as the **increased flux linkage of litz wire** relative to a filament loop.

Due to this, and the violation of (A1), the conventional ac-resistance approach used to model transformers and inductors is insufficient for maglev applications, as the properties of the litz wire cannot be separated from the source field and the circuit's 3D geometry.

However, the litz wires used in maglev is typically short. It is therefore possible to perform a time harmonic FEM simulation with the 3D geometry of the litz wire and the source field $\mathbf{B}^s$ using only one track loop. The limited geometric complexity of this problem makes it tractable for FEM solvers, as opposed to the transformer and inductor problems with longer wires treated in [83],[87],[88].

6.2 Approximation by filament currents – Criteria

We now return to selecting the location of the filament loop ∂P_n to approximate the litz wire vector current density model with filament currents. To this end, there are three different criteria for choosing ∂P_n: **i**) matching flux coupling between track loops, to determine the self and mutual inductance; **ii**) to minimize the error between the force $\mathbf{F}_n^J$ in (19) and $\mathbf{F}_n^i$ in (20) by choosing ∂P_n^F, and **iii**) matching the linked flux from the source, and thereby minimizing the error between the e.m.f. in (25) and $-d/dt\int_{P_n^\phi}\mathbf{B}^s\cdot d\mathbf{S}$ in (18) by choosing P_n^ϕ. It turns out that the considerations: inductance, force, and flux all give different answers to the "best" location of the filament loop ∂P_n.

For the ease of evaluating $\int_{P_n}\mathbf{B}^s\cdot d\mathbf{S}$ and later analysis, the surface P_n is confined to a rectangle parallel to the $x-z$ plane as shown in Figure 5. In this way, we choose a flat filament loop ∂P_n so the linked flux only

depends on B_y^s. We extend P_n^ϕ in the propulsion direction by $2\Delta\phi$ to account for the increased flux linkage of litz wire[11]. Here, we also choose the lateral width of P_n to be w, the transverse width between sidebar centerlines, so that w is identical in the force and the flux computation. The accuracy of w is of little important as long as we use $\Delta\phi$ to match the source flux.

6.3 Criterion for inductance

The inductance vector in the track $\{l_n\}_{n=-\infty}^{\infty}$, shown in Figure 4, represents inductance between loop currents. Since a loop can consist of stranded and solid material (i.e. in Figure 2 the sidebars are solid conductors while the rungs are litz wire) the loop self and mutual inductances are computed by summing the inductance contribution from the different legs of the circuit[12].

First we focus on the self-inductance of a track leg, which is determined by (23), where $\mathbf{J}_m = \mathbf{J}_n$ and $V_m = V_n$. From (24) we infer that the integral depends strongly on the 3D geometry of the current pattern $\tilde{\mathbf{J}}_m$. In a litz wire cable, $\tilde{\mathbf{J}}_m$ differs from a uniform field along the length of the cable due to the strand transposition, but the conductor stranding makes the skin effect in $\tilde{\mathbf{J}}_m$ less noticeable. Wheras in a solid conductor, $\tilde{\mathbf{J}}_m$ will change considerably with current frequency due to the skin effect. The conclusion to be drawn is:

- *Self-inductances must be computed based on the geometry of the current patter* $\tilde{\mathbf{J}}$ *for both litz wire and solid conductors—filament approximations give significant errors.*

We now turn to the mutual inductance M_{mn} also determined by (23). Since the two volumes V_m and V_n are disjoint, the denominator term $|p - p_0|$ attenuates the errors produced by locating filament current in the conductor centers. Define l as the length of the conductor and d the distance between the conductors. Then

$$M = \frac{\mu_0}{4\pi} \int_{-l/2}^{l/2} \int_{-l/2}^{l/2} \frac{1}{\sqrt{d^2 + (y - y_0)^2}} dy_0 dy + \epsilon, \tag{47}$$

which is computed in [89], p. 31. In fact, for a circular straight conductor with fixed radius r, with current flowing parallel to its length, the magnetic field outside is identical to that of a filament located in the center of the conductor, and the error ϵ of the filament approximation decreases rapidly as d/r increases. The current patterns $\tilde{\mathbf{J}}_m$ and $\tilde{\mathbf{J}}_n$ also play a role here, but the effect diminish as d/r increases.

- *Mutual inductances for conductors closer together than a few times their approximate radius must be computed based on the geometry of current patterns* $\tilde{\mathbf{J}}_m$ and $\tilde{\mathbf{J}}_n$.
- *All other mutual inductances can be computed from filaments located in the center of the conductors.*

A square conductor cross-section has very little effect, which is verified by Maxwell's geometric mean distance method as in [89], Chapter 3.

6.4 Criterion for source flux – Flux window width increase $\Delta\phi$

To estimate the loop e.m.f. using filaments, P_n^ϕ is chosen to match the RHS of (25). This is accomplished by adjusting $\Delta\phi(y, v^x)$ in the surface P_n^ϕ defined by

$$P_n^\phi(\Delta\phi) \triangleq \left\{ (x, y, z) \;\middle|\; \begin{array}{c} x^0 + (D-1)n - \Delta\phi \le x \le x^0 + nD + \Delta\phi \\ y \\ -w/2 \le z \le w/2 \end{array} \right\}. \tag{48}$$

[11] To assume that only B_y^s flux is linked to the track, preserves the propperty that the current inducing flux is normla to the lift force generating flux B_x^s. However, it should be kept in mind that for null-flux systems inplemented in the source field (double-sided source), the so called "zero-sag" induced current increases due to the linked B_x and B_z flux in the litz wire. This is accounted for in α_x^{par}, so that the "zero-sag" current augments the drag force and reduces the L/D-ratio also under this assumption.

[12] This method assumes that $M^{tot} = \sum_m \sum_n \pm M_{mn}$ which ignores the proximity effect, and must be used carefully for solid conductors closely spaced as $\tilde{\mathbf{J}}_m$ and $\tilde{\mathbf{J}}_n$ might be affected by $\mathbf{J}_k$ for $k \neq m$ and n.

Here, $\Delta\phi(y, v^x)$ accounts for the variations in flux linkage due to the geometry of the source field and the litz wire and their relative position, and therefore depends on the levitation height y. The skin effect causes the speed dependence. The function $\Delta\phi(y, v^x)$ can be determined from a series of time harmonic FEM simulations parameterized by $v^x_m \in \left\{v^x_1, v^x_2, \ldots, v^x_{M^{v^x}}\right\}$. So that for each chosen speed v^x_m, $\Delta\phi(y, v^x)$ is fit with a polynomial

$$\Delta\phi(v^x_m, y) = \sum_{q=0}^{Q^\phi} a_{qm} y^q. \tag{49}$$

Since v^x is changing slowly relative to the track currents, the M^{v^x} polynomials in $\Delta\phi(v^x_m, y)$ can be pieced together with any continuous interpolation scheme[13].

6.4.1 Determining $\Delta\phi$ from FEM computations

To obtain the function $\Delta\phi(v^x, y)$, it is necessary to model the litz wire geometry of a track loop n in a FEM time harmonic simulation (frequency $= v^x/\lambda$) with the actual source field $\mathbf{B}^s$. The loop current i^{loop}_n is defined in terms of $\mathbf{J}^{loop}_n$ in (16), and is determined by numerical integration. The inductance coupling $\sum_m l_m d/dt\, i^{loop}_{n+m}$ into loop n in (18) truncates to the self inductance $l_0 d/dt\, i^{loop}_n$ for a single loop, and is also determined by numerical integration (for instance according to (23)).

The $\Delta\phi(y, v^x)$ is determined by equating the average e.m.f. $R^{loop}_n i^{loop}_n$ (25) with the filament loop approximation (18) by adjusting the flux region $P^\phi_n(\Delta\phi)$ (48). This is carried out at a grid of levitation heights $y_k \in \{y_1, y_2, \ldots, y_{K^\phi}\}$, $K^\phi > Q^\phi$ (for a fixed v^x) as

$$\min_{\Delta\phi_k} \left(R^{loop}_n i^{loop}_n(y_k) \;+\; \frac{d}{dt} \int\limits_{P^\phi_n(y_k, \Delta\phi_k)} B^s_y \, dxdz \;+\; l_0 \frac{d}{dt} i^{loop}_n \right), \tag{50}$$

The result is the set $\{\Delta\phi_1, \Delta\phi_2, \ldots, \Delta\phi_{K^\phi}\}$ which is used to fit the coefficients $\left\{a_{0m}, a_{1m}, \ldots, a_{Q^\phi m}\right\}$ in (49) for one v^x_m. Any coefficient fitting method (e.g. least squares) can be used.

- *The parameter $\Delta\phi(y, v^x)$ is determined from 3D FEM simulation incorporating the precise track and cable geometry in addition to the source field geometry by performing the optimization (50) and fitting the functions (49)*

6.5 Criterion for force – Effective force levitation height y^F

For a single-sided source it is sufficient to use only one filament location ∂P^F_n to compute the force as explained in Appendix B.2. Thus, it suffices to use $y^F \triangleq y - \Delta y^F$ to minimize the error ϵ_F in the force approximation criterion between the actual force $\mathbf{F}^J_n$ in (19) and the filament approximation $\mathbf{F}^i_n$ in (20). The force criterion becomes the minimization of ϵ_F by choosing Δy^F in

$$\mathbf{F}_n(y^F) \;=\; \int\limits_{V^{loop}_n} \mathbf{J}^{loop}_n \times \mathbf{B}^s dV \tag{51}$$

$$\;=\; \int\limits_{\partial P^F_n(\Delta y^F)} i^{loop}_n d\mathbf{l} \times \mathbf{B}^s \;+\; \epsilon_F \tag{52}$$

where (51) is the actual force and (52) is the filament approximation. The distance from the body fixed frame at the lower edge of the source to the vertical center of a rung, y, is shown in Figure 6. The surface P^F_n is given

[13] For instance, to interpolate between two values $\Delta\phi(v^x_1, y)$ and $\Delta\phi(v^x_2, y)$ in the range $v_x \in [v^x_1, v^x_2]$, use the scheme $\Delta\phi(v^x, y) = 1/(v^x_2 - v^x_1)\left[\Delta\phi(v^x_1, y)(v^x_2 - v^x) + \Delta\phi(v^x_2, y)(v^x - v^x_1)\right]$.

by

$$P_n^F(y^F) \triangleq \left\{ (x,y,z) \;\middle|\; \begin{array}{c} x^0+(D-1)n \le x \le x^0+Dn \\ y^F = y - \Delta y^F \\ -w/2 \le z \le w/2 \end{array} \right\}. \tag{53}$$

For a single relative position between $\mathbf{J}_n^{loop}$ and $\mathbf{B}^s$, the optimal location of ∂P_n^F may not go through the horizontal center of a track rung. But if we average over all horizontal source positions, the filament contour ∂P_n^F runs through the horizontal center of a track rung x^0. An unbiased horizontal filament position for the total force from all track loops, is therefore $x^0 + Dn$. Whence the choice of x^0 in (53).

Similar to $\Delta\phi$, the function $\Delta y^F(v^x, y)$ is determined at a set of propulsion velocities $v_m^x \in \left\{v_1^x, v_2^x, \ldots, v_{M^{v^x}}^x\right\}$. So that for each chosen speed v_m^x the parameterization is

$$\Delta y^F(v_m^x, y) = \sum_{q=0}^{Q_F} b_{qm} y^q, \tag{54}$$

and the M^{v^x} polynomials are interpolated with any continuos scheme as in (49).

6.5.1 Determining Δy^F from FEM computations - no assumption of current equalization

In computing Δy^F using a time harmonic FEM simulation, it is necessary to include the geometry of both the track cable and $\mathbf{B}^s$, for a single track loop n. The function $\Delta y^F(y, v^x)$ is determined by a minimization of the difference between the numerically integrated force in (51) and the force from the filament loop (52) by adjusting $\Delta y^F(y_n)$. The loop current i_n^{loop} is given by (16). This is carried out at a grid of levitation heights $y_k \in \{y_1, y_2, \ldots, y_{K^F}\}$, $K^F > Q^F$ for fixed v_m^x as

$$\min_{\Delta y_k^F} \left\| \int_{V_n^{loop}} \mathbf{J}_n^{loop} \times \mathbf{B}^s(y_k)\, dV \;-\; \int_{\partial P_n^F(y_k - \Delta y_k^F)} i_n^{loop} d\mathbf{l} \times \mathbf{B}^s \right\|_2 . \tag{55}$$

The result is the set $\{\Delta y_1^F, \Delta y_2^F, \ldots, \Delta y_{K^F}^F\}$ which is used to fit the coefficients $\left\{b_{0m}, b_{1m}, \ldots, b_{Q^F m}\right\}$ in (49) for one v_m^x. Any coefficient fitting method (e.g. least squares) can be used.

- *The best filament position for force computation for single-sided sources is $\partial P_n^F(y^F)$ (53), where $\Delta y^F(v_m^x, y)$ is determined by (55) from 3D time harmonic FEM simulations.*

6.5.2 Double-sided sources Δy^{Fl} and Δy^{Fd}

As explained in Appendix B.2, for double-sided sources, we have to use separate vertical filament locations y^{Fl} and y^{Fd} for the lift and the drag force, respectively, and determine the functions

$$\Delta y^{Fl}(v_m^x, y) = \sum_{q=0}^{Q^F} b_{qm} y^q \tag{56}$$

$$\Delta y^{Fd}(v_m^x, y) = \sum_{q=0}^{Q^F} c_{qm} y^q, \tag{57}$$

independently. The fitting procedure described in Section 6.5 and 6.5.1 still applies, but (56) is determined from the minimization over the set of levitation heights $y_k \in \{y_1, y_2, \ldots, y_{K^F}\}$ for fixed v_m^x as

$$\min_{\Delta y_k^{Fl}} \left\| \hat{\mathbf{e}}_y \cdot \left(\int_{V_n^{loop}} \mathbf{J}_n^{loop} \times \mathbf{B}^s(y_k)\, dV \;-\; \int_{\partial P_n^F(y_k - \Delta y_k^{Fl})} i_n^{loop} d\mathbf{l} \times \mathbf{B}^s \right) \right\|_2 , \tag{58}$$

while (57) is found from

$$\min_{\Delta y_k^{Fd}} \left\| \hat{\mathbf{e}}_x \cdot \left(\int_{V_n^{loop}} \mathbf{J}_n^{loop} \times \mathbf{B}^s(y_k)\, dV - \int_{\partial P_n^F(y_k - \Delta y_k^{Fd})} i_n^{loop} d\mathbf{l} \times \mathbf{B}^s \right) \right\|_2 , \tag{59}$$

and the resulting sets $\{\Delta y_1^{Fl}, \Delta y_2^{Fl}, \ldots, \Delta y_{K^F}^{Fl}\}$ and $\{\Delta y_1^{Fd}, \Delta y_2^{Fd}, \ldots, \Delta y_{K^F}^{Fd}\}$ are used to fit the coefficients $\{b_{0m}, b_{1m}, \ldots, b_{N^F m}\}$ and $\{c_{0m}, c_{1m}, \ldots, c_{N^F m}\}$, respectively.

- *For double-sided sources, the filament location for the lift force $\partial P_n^F(y^{Fl})$ is different from the filament location for the drag force $\partial P_n^F(y^{Fd})$.*

In the next Section, we assume current equalization (A1), which simplifies the effective force levitation height to a 2D problem where y^F is independent of the levitation height. In fact we get $\Delta y^F(v_m^x) = b_{0m}(v_m^x)$.

6.5.3 Δy^F under assumption of current equalization

With current equalization (A1), we will explain that Δy^F decreases relative to (55) for single-sided sources and will be zero for double-sided sources.

First, we make the technical assumptions on the litz wire implicitly made in [84]-[86]:

Assumption 3 ***Cross-section symmetry***
The strands are symmetrically distributed around the center of the cross-section.

For maglev applications, the conductor thickness is more than one order of magnitude less than the horizontal dominant spatial wavelength of the source λ. Consequently, the horizontal magnetic flux density $\mathbf{B}_y^s$ is approximately constant over the conductor, and we assume the same 1-D ($y-$direction) source field as in [85]:

Assumption 4 ***Horizontal field invariance***
For x inside a conductor, $\mathcal{B}_y^s(x,y) = \mathcal{B}_y^s(x^0, y)$, where x^0 is the horizontal center of a rung.

Current equalization (A1) and cross-section symmetry (A3) impliy that the total current is directed along the axis, more precisely, $\int_A \mathbf{J} dA = i^{rung} \hat{\mathbf{e}}_z$ at all cross-section positions along a litz wire. It therefore suffices to derive the force for the cross-section shown in Figure 6 between a rung current i^{rung} and $\mathbf{B}^s$. This force is approximated by the sum of the forces between the strand currents $i_{k,l}^{rung}/N$ and the magnetic flux at the location of the strand filaments $\mathcal{B}_{\delta c(m,n)}^s$ with δc as the distance between strand centers

$$\mathbf{F} = \int_{V_c} \mathbf{J} \times \mathbf{B}^s dV \approx \sum_k^{width} \sum_l^{height} \frac{i_{k,l}^{rung}}{N} \hat{\mathbf{e}}_z \times \mathcal{B}_{\delta c(m,n)}^s. \tag{60}$$

Thus, we replace each strand by a filament conductor in the center, which gives identically the same lift force if the current density in each strand is uniform, and (A2) is assumed. We employ (A1) to bring i^{rung} outside the summation, and (60) becomes

$$\begin{aligned} \mathbf{F} &= \frac{i^{rung}}{N} \hat{\mathbf{e}}_z \times \sqrt{N} \sum_{l=-\sqrt{N}/2}^{\sqrt{N}/2-1} \mathcal{B}^s(x^0, y + \delta c\, l) \\ &\triangleq \frac{i^{rung}}{N} \hat{\mathbf{e}}_z \times N \mathcal{B}^s(x^0, y^F), \end{aligned} \tag{61}$$

where the width summation collapses since $\mathcal{B}_y^s(x,y) = \mathcal{B}_y^s(x^0, y)$ by (A4), and the last line is the defining equation for the filament location (x^0, y^F). To determine y^F, we solve (61) for $\Delta y^F = y - y^F$ by using the inverse $\mathcal{B}^{s-1}$

in the y-coordinate and obtain

$$\Delta y^F = y - \mathcal{B}^{s-1}\left(x^0,\, \tfrac{1}{\sqrt{N}} \sum_{l=-\sqrt{N}/2}^{\sqrt{N}/2-1} \mathcal{B}^s\left(x^0, y+\delta c\, l\right)\right). \tag{62}$$

If $\mathcal{B}^s(\cdot, y')$ is a <u>linear</u> function of y' in the range over the conductor $y' \in [y - \delta c\sqrt{N}/2, y + \delta c(\sqrt{N}/2-1)]$, we have

$$\begin{aligned} \mathcal{B}^{s-1}\left(\tfrac{1}{\sqrt{N}} \sum_{l=-\sqrt{N}/2}^{\sqrt{N}/2-1} \mathcal{B}^s\left(y+\delta c\, l\right)\right) &= \tfrac{1}{\sqrt{N}} \sum_{l=-\sqrt{N}/2}^{\sqrt{N}/2-1} \mathcal{B}^{s-1}\mathcal{B}^s(y+\delta c\, l) & (63)\\ &= \tfrac{1}{\sqrt{N}} \sum_{l=-\sqrt{N}/2}^{\sqrt{N}/2-1} y+\delta c\, l \quad = \quad y & (64) \end{aligned}$$

where the last line followed from $f^{-1}(f(y)) = y$. For a double-side source, $\mathcal{B}^s_y(\cdot, y')$ is approximately a linear function in y' as demonstrated in Appendix B.1. Hence, Δy^F is zero for a double-sided source.

- *Under the assumption of current equalization (A1), for double-sided sources,* $\Delta y^{Fl} = \Delta y^{Fd} = 0$.

For a single-sided source, Δy^F is nonzero with the explicit solution of (62) given by (78) in Appendix B.1. Differently stated, under current equalization the functions (54),(56) and (57) simplifies to constants. From this we conclude:

- *The degree to which* $\Delta y^F, \Delta y^{Fl}$ *and* Δy^{Fd} *are independent of* y*, reflects to what extent the current equalization is achieved.*

6.6 Dynamic considerations of the criteria

So far, the criteria for inductance, force and flux have been considered under quasi-stationary conditions with constant v^x. That is, the spectral content of the source $\nabla_{\mathbf{p}}\mathbf{B}^s \cdot d\mathbf{p}/dt'$ in (11), and thus the induced current $\mathbf{J}$, are constant. This is equivalent to constant speed $d\mathbf{p}/dt = v^x\hat{\mathbf{e}}_x$. If the acceleration $d^2\mathbf{p}/dt^2$ is moderate, the spectral content of $\mathbf{J}$ changes slowly, so we anticipate the quasi-stationary assumptions to hold even here when we have parameterized the criteria on v^x.

It is when $d^2\mathbf{p}/dt^2$ is large, that the quasi-stationary conditions may fail, as in [61], from alterations in the current vector field pattern $\tilde{\mathbf{J}}$. However, the conductor stranding in litz wire restricts how large the variations in $\tilde{\mathbf{J}}$ can be from skinning, proximity effect, and eddy currents. This is the major advantage of stranded conductors over solid conductors where $\tilde{\mathbf{J}}$ changes considerably with $d^2\mathbf{p}/dt^2$. We conclude:

- *If the portion of the track contributing the significant part of the force is stranded, the criteria for inductance flux and force can be generalized to include considerable acceleration with good accuracy.*

Since v^x and y are varying slowly compared to the currents in the model, the dependency of $\Delta\phi(y, v^x)$ and $\Delta y^F(y, v^x)$ on y and v^x are at most slowly time varying, so that all derivatives with respect to y and v^x are insignificant. That is, $\partial_{v^x}\Delta\phi(y, v^x) \approx 0$ etc. This assumption is justified by two-scale separation between the fast current equation and the slow mechanical equation which occurs below the propulsion velocity where the lift force equals the drag force.

7 Energy and power – including parasitic dissipation from eddy currents

We need to account for the induced eddy currents within strands of the litz wire and in surrounding low resistivity material which are labeled *parasitic currents* $\mathbf{J}^{par}$. Eddy currents arise from flux gradients moving

across a conductor and have the effect of *shielding* the conductor and create *ohmic losses* $\int \rho \left|\mathbf{J}^{par}\right|^2 dV$. We don't include this shielding effect in the current equation in Section (5), but instead compensate for the resulting force $\mathbf{F}^{par}$ from parasitic currents using power loss as

$$\mathbf{F}^{par} = \boldsymbol{\alpha}^{par} \cdot \frac{d\mathbf{p}}{dt}. \tag{65}$$

To resolve this loss, we inquire into the system energy, and label the track currents $\mathbf{J}^i$, the source currents $\mathbf{J}^s$, and the parasitic loss currents in the inertial frame $\mathbf{J}^{par}$ and the moving frame $\mathbf{J}^{'par}$, respectively. These currents have corresponding magnetic vector potentials $\mathbf{A}^i$, $\mathbf{A}^s$, $\mathbf{A}^{par}$, and $\mathbf{A}^{'par}$. By introducing the index set $\mathcal{N} = \{i, s, par, ' par\}$, the total magnetic energy is

$$E^J = \tfrac{1}{2} \sum_{k \in \mathcal{N}} \sum_{l \in \mathcal{N}} \int_{V^{J^l}} \mathbf{A}^k \cdot \mathbf{J}^l dV. \tag{66}$$

Expanding the sum, simplifying the cross terms as $\int_{V^{J^l}} \mathbf{A}^k \cdot \mathbf{J}^l dV = \int_{V^{J^k}} \mathbf{A}^l \cdot \mathbf{J}^k dV$, and replacing $\mathbf{J}^i$ with $i\{n\}$ yields

$$\begin{aligned}
E^J \;=\; & \underbrace{\tfrac{1}{2} \sum_{n=-\infty}^{\infty} \sum_{m=-\infty}^{\infty} \int_{V_n^i} \mathbf{J}_n^i \cdot \mathbf{A}_m^i}_{(1)} \;+\; \underbrace{\sum_{n=-\infty}^{\infty} \int_{V_n^i} \mathbf{J}_n^i \cdot \mathbf{A}^s dV}_{(2)} \\
& + \underbrace{\tfrac{1}{2} \int_{V^s} \mathbf{J}^s \cdot \mathbf{A}^s dV}_{3)} \;+\; \underbrace{\sum_{n=-\infty}^{\infty} \int_{V_n^i} \mathbf{J}_n^i \cdot \mathbf{A}^{par} dV}_{(4)} \\
& + \underbrace{\int_{V^s} \mathbf{J}^s \cdot \mathbf{A}^{par} dV}_{(5)} \;+\; \underbrace{\sum_{n=-\infty}^{\infty} \int_{V_n^i} \mathbf{J}_n^i \cdot \mathbf{A}^{'par} dV}_{(6)} \\
& + \underbrace{\int_{V^s} \mathbf{J}^s \cdot \mathbf{A}^{'par} dV}_{(7)} \;+\; \underbrace{\int_{V^{par}} \mathbf{J}^{par} \cdot \mathbf{A}^{'par} dV}_{(8)} \\
& + \underbrace{\tfrac{1}{2} \int_{V^{par}} \mathbf{J}^{par} \cdot \mathbf{A}^{par} dV}_{(9)} \;+\; \underbrace{\tfrac{1}{2} \int_{V^{'par}} \mathbf{J}^{'par} \cdot \mathbf{A}^{'par} dV}_{(10)}
\end{aligned} \tag{67}$$

The first term is the track current energy $1/2 \sum_{n=-\infty}^{\infty} \sum_{m=-\infty}^{\infty} i_n l_{m-n} i_m = 1/2 \left\langle i\{n\}, \mathcal{L} i\{n\} \right\rangle_n$; the second term is the energy in the coupling between the source and the track which can be expressed as $\sum_n i_n \Phi_n = \left\langle i\{n\}, \Gamma^x_{\Delta\phi}\{nD\} \int_{P^\phi} \mathcal{B}^s_y(x', y) dx' \right\rangle_n$ from (27) and (31); the third term is the constant magnetic source energy; terms four to seven are the interaction energies between the parasitic current, the track, and the source; term eight is interaction energy between the parasitic currents, and term nine and ten are the self energies of the parasitic currents. A necessary condition for our modelling to be successful is:

- *The modelled terms one through three are large compared to the sum of the omitted terms four to ten.*

The terms four, seven, nine, and ten, where both $\mathbf{A}$ and $\mathbf{J}$ are in the same frame, are independent of $\mathbf{p}$ and do not cause a force between the levitated object an the track. Only the interaction terms two, five, six, and eight generate a force between the levitated object and the track, where in particular term six can produce a significant *parasitic vertical damping force* $\alpha_y^{par} dy/dt$ ($\alpha_y^{par} > 0$) depending on the geometry of $\mathbf{J}'^{par}$ [90],[37]. The parasitic

currents induced by propulsion motion similarly produce a *parasitic drag force* $\alpha_x^{par} dx/dt$ ($\alpha_x^{par} > 0$). The power loss of $\mathbf{J}^{par}$ and $\mathbf{J}'^{par}$ averaged over the interval $[0, T]$ defines the *parasitic dissipation force* $\boldsymbol{\alpha}^{par} \cdot d\mathbf{p}/dt$ as

$$\frac{1}{T}\int_{\mathbf{p}(0)}^{\mathbf{p}(T)} \boldsymbol{\alpha}^{par} \cdot d\mathbf{p} \;\triangleq\; \frac{1}{T}\int_0^T\int_{V^{Jpar}} \rho^{par} \left|\mathbf{J}^{par}\right|^2 dV\, dt \;+\; \frac{1}{T}\int_0^T\int_{V^{J'par}} \rho'^{par} \left|\mathbf{J}'^{par}\right|^2 dV\, dt. \tag{68}$$

Since the inherent vertical damping in (43)-(45) is negative above a certain propulsion velocity, accounting for the parasitic damping $\alpha_y^{par} dy/dt$ is crucial. The presence of parasitic damping should not be confused with the inherent stability of (43)-(45) in the absence of parasitic damping.

For the double-sided source, the parasitic drag force accounts for the so-called "zero-sag" drag (the drag force when the lift force is zero) which limits the achievable L/D-ratio contrary to the over simplified (82) and Figure 11 in Appendix B.2.

To verify the applicability and limitations of (68), we must investigate the electromagnetic power balance.

7.1 Electromagnetic energy and power balance

Under quasistatic conditions, without free charge, the electromagnetic energy is ${}^{EM}E = {}^{J}E$ (66). The input magnetic energy ${}^{EM}E^{in}$ transferred from the mechanical energy over the time interval $[0, T]$ is

$${}^{EM}E^{in}(T) = \int_0^T \frac{\partial}{\partial \mathbf{p}}\, {}^{J}E \cdot \frac{d\mathbf{p}}{dt} dt, \tag{69}$$

where a positive sign of ${}^{EM}E^{in}$ is associated with increase in electromagnetic energy. Equation (69) is the integral of the generalized magnetic force times (dot product) the velocity $d\mathbf{p}/dt$, which is a non-conservative force since ${}^{J}E$ depends explicitly on time through the currents. The dissipated electromagnetic energy is the resistive loss ${}^{EM}E^{diss}(T) = \sum_{k\in\mathcal{N}} \int_0^T \int_{V^{J_k}} \rho_k \left|J_k\right|^2 dV\, dt$. The electromagnetic energy balance over $[0, T]$ becomes

$${}^{EM}E^{in}(T) = {}^{EM}E^{stored}(T) + {}^{EM}E^{diss}(T). \tag{70}$$

By taking time derivatives of (70) and using (66), the electromagnetic power balance is

$$\frac{\partial}{\partial \mathbf{p}} \left(\tfrac{1}{2} \sum_{k\in\mathcal{N}} \sum_{l\in\mathcal{N}} \int_{V^{J_l}} \mathbf{A}^k \cdot \mathbf{J}^l dV \right) \cdot \frac{d\mathbf{p}}{dt} \tag{71}$$

$$= \quad \frac{d}{dt} \tfrac{1}{2} \sum_{k\in\mathcal{N}} \sum_{l\in\mathcal{N}} \int_{V^{J_l}} \mathbf{A}^k \cdot \mathbf{J}^l dV \;+\; \sum_{k\in\mathcal{N}} \int_{V^{J_k}} \rho_k \left|J_k\right|^2 dV. \tag{72}$$

It is customary, even for discrete tracks, to ignore the first term in RHS of (72) and set the magnetic drag force $F^d dx/dt \approx \sum_{k\in\mathcal{N}} \int_{V^J} \rho_k \left|J_k\right|^2 dV$. This completely ignores the power flow into or out of the magnetic field. In addition, the vertical magnetic damping force is not accounted for. The consequence is a model with unstable heave oscillations. In contrast, the oscillations would have been less dominant, possibly stable, or altogether disappeared if the damping was included.

Define

$$\varepsilon(T) \;\triangleq\; \tfrac{1}{2} \tfrac{1}{T} \sum_{k\in\mathcal{N}} \sum_{l\in\mathcal{N}} \int_{V^{J_l}} \mathbf{A}^k \cdot \mathbf{J}^l dV \,\Bigg|_{t=0}^{T}, \tag{73}$$

take the time average over $[0, T]$ of (72), noticing that $\mathbf{F} = \mathbf{F}^s + \boldsymbol{\alpha}^{par} \cdot d\mathbf{p}/dt$, and we obtain the averaged magnetic power balance

$$\frac{1}{T} \int_{\mathbf{p}(0)}^{\mathbf{p}(T)} \mathbf{F} \cdot d\mathbf{p} = \varepsilon(T) + \sum_{k\in\mathcal{N}} \int_0^T \int_{V^J} \rho_k \left|J_k\right|^2 dV\, dt. \tag{74}$$

If the solution to (43)-(45) undergoes "periodic motion"[14], as $(i\{n\}(t), y(t)) = (i\{n\}(t+T), y(t+T))$, we have that $\varepsilon(t) \overset{t\to T}{\longrightarrow} 0$. However, the average of the first RHS term of (72) is nonzero when the motion is aperiodic, such that $\mathbf{p}(0)$ and $\mathbf{p}(T)$ correspond to different mechanical energies indicating that there has been a change in mechanical energy on the account of $\varepsilon(T)$. That is, under strong acceleration $\int_{\mathbf{p}(0)}^{\mathbf{p}(T)} d^2\mathbf{p}/dt^2 \cdot d\mathbf{p} \gg 0$, the modelled parasitic dissipation $\boldsymbol{\alpha}^{par} \cdot d\mathbf{p}/dt$ (68) is too small since $\varepsilon(T) \gg 0$ in (74), and under strong retardation $\boldsymbol{\alpha}^{par} \cdot d\mathbf{p}/dt$ is too large since $\varepsilon(T) \ll 0$. This is in agreement with the hysteresis cycles under acceleration found in [61], but any such cycles will be marginal if litz wire is used throughout as explained in Section 6.6.

However, for the natural heave resonance the acceleration is moderate, and the heave dynamics will be preserved. So we conclude:

- *Using the parasitic dissipation (68) with $T = D/v^x$, the dynamics of the ITM (43)-(45) are identical to (11) and (14) in a neighbourhood of the natural heave resonance.*

8 Conclusion

We have derived general governing equations for discrete track electrodynamic suspension (EDS) maglev from Maxwell's Equations, carefully stating the underlying assumptions. We have arrived at equations (43)-(45), called the Infinite Track Model (ITM), unifying both dynamic and static properties. The ITM has a similar structure as continuous track EDS maglev: A mechanical equation (ODE) expresses the rigid body dynamics of the levitated object, and an infinite dimensional current equation describes the track currents, which is diffusion (11) for continuous tracks and discretized diffusion on a line (43) for discrete tracks. The diffusion source-term depends on position and velocities of the rigid body, and is determined by the degrees of freedom which determine the interpretation of the derivative (1) in Faraday's Law. The ITM has the following features:

- The mutual inductance between track conductors creates discrete convolution operators (35) which replace the Laplacian in the diffusion equation (11) for continuous tracks.
- The filament approximation criteria for inductance, force, and flux considerations give different results as to where the filament current should be located. Varying current vector field pattern in the track creates parameter dependent criteria as well as parameter dependent track operators.
- A limited amount of eddy currents within conductor strands, and induced currents in surrounding low resistivity material can be compensated for using parameter dependent power loss, increasing the drag force and the heave damping. The averaged dynamic error of this modelling is zero near periodic orbits.

8.1 Acknowledgements

The authors whish to thank the General Atomics' urban maglev development team for fruitful discussions and generous information sharing. We would also like to thank Dr. Richard Post at Lawrence Livermore National Laboratory for his contribution to this research at its early stages. This material is based upon work supported by the National Science Foundation under Grant no. CMS-0220386.

[14] Here, we must allow all cyclic permutations of $i\{n\}$ to be equivalent to have periodic motion when for instance the levitated object has moved the distance between two track rungs D, such that $T = D/v^x$.

Appendix

A Energy and Power

A.1 Equivalent expressions for energy under quasistatic conditions

We start from the expression for magnetic energy, where the volume integral is taken over all of space

$$E^J = \tfrac{1}{2}\int_{\mathbb{R}^3} \mathbf{B}\cdot\mathbf{H}dV. \tag{75}$$

We must interpret both integral and differential operators in the sense of distributions to account for possible discontinuity effects at surfaces. Using the vector identity $(\nabla\times\mathbf{G})\cdot\mathbf{F} = -\nabla\cdot(\mathbf{F}\times\mathbf{G}) + (\nabla\times\mathbf{F})\cdot\mathbf{G}$, where $\mathbf{F},\mathbf{G}:\mathbb{R}^3\to\mathbb{R}^3$ are arbitrary vector fields, and the magnetic vector potential $\mathbf{A}$ is defined as $\mathbf{B} = \nabla\times\mathbf{A}$, (75) becomes

$$E^J = -\tfrac{1}{2}\int_{\mathbb{R}^3} \nabla\cdot(\mathbf{H}\times\mathbf{B})dV + \tfrac{1}{2}\int_{\mathbb{R}^3}(\nabla\times\mathbf{H})\cdot\mathbf{A}dV. \tag{76}$$

The first integral is zero if the permeability $\mathbf{B} = \mu\mathbf{H}$ is a continuous function in all of space (otherwise there will be singular terms at the sets of discontinuity). Since we have ignored displacement current, Ampere's circuit Law (4) is $\nabla\times\mathbf{H} = \mathbf{J}$, and the last integral simplifies to

$$E^J = \tfrac{1}{2}\int_{V^J} \mathbf{J}\cdot\mathbf{A}dV, \tag{77}$$

where the integral is now only over the volume of the current V^J, which is the advantage in using (77) over (75).

B Litz wire

B.1 Evaluating Δy^F under current equalization

For the single sided-source, we approximating the y-dependence of the magnetic field as $\mathbf{B}(\cdot,y)\sim e^{-ky}$ as in the "semi-quantitative computations" of [28], and use the finite summation formula for geometric series to obtain

$$\Delta y^F = \frac{1}{k}\ln\left(\frac{e^{-k\delta y\sqrt{N}}-1}{\sqrt{N}(e^{-k\delta y}-1)}\right). \tag{78}$$

For the double-sided source, we again approximate the y-dependence of the magnetic field from two single sided source as $\mathbf{B}(\cdot,y)\sim e^{-ky}$ and get

$$\mathbf{B}(y) \sim B_{0u}e^{-ky} - B_{0l}e^{-k(2h-y)}, \tag{79}$$

where the coordinate origin is at the lower edge of the upper source, and $2h$ is the gap between the sources. If the *zero vertical flux height* y^*, defined as $B_y(y^*) = 0$, is between the sources, then B_{0l}/B_{0u} is approximately in the range 1 to $4h/\lambda$, and a linear approximation is very good as shown in Figure 10. Consequently, Δy^F under current equalization (A1) is zero for double-sided sources for all values of y.

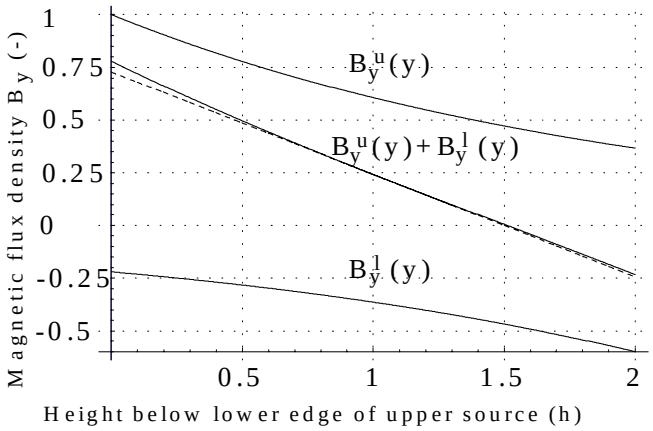

Figure 10: Vertical magnetic field from a two-sided source with $B_{0l}/B_{0u} = 0.6$ where the linearization is the dashed line. The magnetic field is approximated with exponentials as: $B_y^u(y) = e^{-ky}$, $B_y^l(y) = -0.6e^{-k(2h-y)}$, where $h = 70\ mm$ and $k = 14.32\ rad/m$. The linearization is taken at $y = h$, and $y^* = 1.509\ h$. If the conductor thickness is $20\ mm = 0.285\ h$, the linear approximation is very good inside the conductor.

B.2 y^F for single-sided and double-sided sources

To motivate the essential difference between single-sided and double-sided sources, we will first confine our treatment to a double-sided, periodic, symmetric (upper and lower sources are equally strong), and infinitely wide source to justify a 2D treatment of $\mathbf{B}^s(x, y)$. If we also ignore the end effect, and assume an infinitely long source, the problem can be treated with lumped parameters analogous to the "semi-quantitative calculations" in [28]. In this setting, the track is located in the gap between the sources, and has equivalent one-loop inductance L_{eq} and resistance R_{eq}, whereas the upper and lower sources have a fundamental spatial wavelength λ. The wave number for the horizontal fundamental wavelength is $k = 2\pi/\lambda$, and we disregard higher harmonics. If the distance between the sources is $2h$, the magnetic flux density is

$$\mathbf{B}^s(x, y) \sim e^{-kh} \left(\sin(kx)\cosh(ky)\hat{\mathbf{e}}_x + \cos(kx)\sinh(ky)\hat{\mathbf{e}}_y\right), \tag{80}$$

which is stated as the magnetic field from a Halbach array in [29], but has general validity under the stated conditions due to the solution of Poisons's Equation $\Delta\mathbf{A} = -\mu\mathbf{J}$ for a static current $\mathbf{J}$, where $\mathbf{B} = \nabla \times \mathbf{A}$. The lift-to-drag ratio is

$$\frac{F^l}{F^d} = \frac{1}{\tanh(k[y-h])}\frac{kL_{eq}}{R_{eq}}v^x, \tag{81}$$

which is approximated, using the absolute value function $|\cdot|$, as

$$\frac{F^l}{F^d} \approx \frac{1}{k\,|y-h|}\frac{kL_{eq}}{R_{eq}}v^x, \tag{82}$$

The comparison between (81) and (82) is plotted as drag-to-lift ratio in Figure 11, to reveal a near linear dependence on y.

For single-sided sources, the hyperbolic terms in (80) disapears, and the term $\tanh(k[y-h]) = 1$, and the L/D ratio is in first approximation independent of levitation height y. Thus, it is possible to compute the force from a single filament location as $\mathbf{F} = \int_{\partial P_n^F(y^F)} i^{loop} d\mathbf{l} \times \mathbf{B}^s$. Notice however, that without approximations, k in (82) depends weakly on y through the end effect, so $y^F(y)$ is a weak function of the levitation height y for single-sided sources as well.

For a double-sided source, the lift-to-drag ratio depends strongly on the levitation height y, and from Figure 11 we infer that there is only one vertical position of the filament $y^{L/D}$ (above y^*) that yields the correct L/D

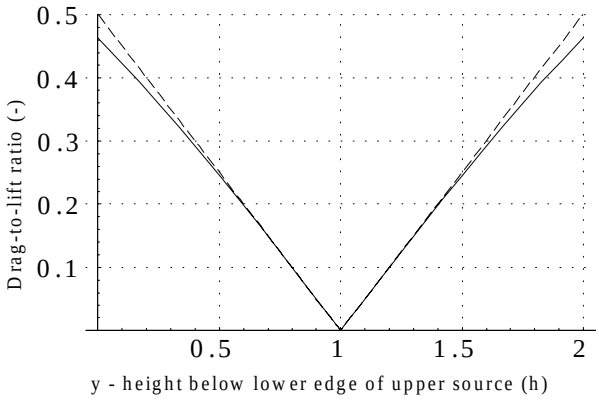

Figure 11: The drag-to-lift ratio for a double-sided, infinitely wide source (solid), ignoring the end effect and higher order harmonics. The linear approximation (dashed) is very good around the zero vertical flux height $y^* = h$, which is close to the desirable operation range.

ratio. Simultaneously, the magnitude in either the lift or the drag force should match that of the vector current density model, which is, due to the 3D litz wire and source field geometry, not necessarily attainable at the levitation height $y^{L/D}$. From this dimensional argument, it becomes necessary to compute the lift force as

$$F^l = \hat{\mathbf{e}}_y \cdot \int_{\partial P_n^F(y^{Fl})} i^{loop} d\mathbf{l} \times \mathbf{B}^s \tag{83}$$

and the drag force from

$$F^d = \hat{\mathbf{e}}_x \cdot \int_{\partial P_n^F(y^{Fd})} i^{loop} d\mathbf{l} \times \mathbf{B}^s. \tag{84}$$

In other words, for double-sided sources, the lift and drag forces can not necessarily be computed from a single filament as this would be an exceptional case due to the 3D geometry of the track and the source field.

C The time varying part of the mirror magnetic field

Our aim is to derive the growth rate of the time-varying part of the mirror magnetic field $\mathbf{B}^m(t)$ in the moving reference frame as a function of the ratio D/λ. We confine our treatment to a single-sided source, periodic in the propulsion direction, and ignore the end effect. This setting permits using a lumped parameter model with equivalent track inductance L_{eq} and resistance R_{eq} when solving for the loop currents i_n. We further assume a constant propulsion speed v^x and constant levitation height y. The wave number for the horizontal fundamental wavelength is again $k = 2\pi/\lambda$, and we disregard higher harmonics.

If $\mathcal{B}^0$ is a proportionality coefficient determined by the width of the track and the source geometry, the transversely integrated magnetic field from the single-sided source is

$$\mathcal{B}^s(x, y) = \mathcal{B}^0 e^{-ky} \left[\sin(kx)\hat{\mathbf{e}}_x + \cos(kx)\hat{\mathbf{e}}_y\right]. \tag{85}$$

Considering filament currents in the track, the e.m.f. in track loop n can be written

$$E_n = v^x \mathcal{B}^0 e^{-ky} \left[2\sin(\pi\tfrac{D}{\lambda})\sin(kv_x t - \pi\tfrac{D}{\lambda}(2n-1)\right]. \tag{86}$$

Defining the characteristic velocity v^c as the propulsion speed where the lift force equals the drag force

$$v^c \triangleq \frac{R_{eq}}{kL_{eq}}, \tag{87}$$

we find the track current i_n using the equivalent track circuit with lumped parameters L_{eq} and R_{eq} an obtain

$$\begin{aligned} i_n(t) &= B' 2\sin(\pi\tfrac{D}{\lambda}) \times \\ &\quad \left[\cos(kv_{xt} - 2\pi\tfrac{D}{\lambda}n) - \frac{v^c}{v^x}\sin(kv_x t - 2\pi\tfrac{D}{\lambda}n) - e^{-\frac{R_{eq}}{L_{eq}}t}\right], \end{aligned} \tag{88}$$

where the coefficient B' is

$$B' \triangleq \frac{\mathcal{B}^0 e^{-ky} v^c}{R_{eq}} \frac{1}{1+\left(\frac{v^c}{v^x}\right)^2}. \tag{89}$$

We assume that v^c/v^x is small, so that the term $(v^c/v^x)\sin(kv_x t - 2\pi\frac{D}{\lambda}n)$ in (88) can be ignored together with the initial response $e^{-\frac{R_{eq}}{L_{eq}}t}$, and only the first term $\cos(kv_{xt} - 2\pi\frac{D}{\lambda}n)$ remains. The rung current $i_n^{rung} = i_n - i_{n-1}$ now becomes

$$i_n^{rung} = -B' 4\sin^2(\pi\tfrac{D}{\lambda})\sin(kv_x t - \pi\tfrac{D}{\lambda}(2n-1)). \tag{90}$$

Since we are dealing with densely spaced tracks, the magnetic flux density contribution from the sidebars is omitted. If each rung filament has length w, and $\hat{\mathbf{e}}_{\theta n}(x,y)$ is the unit vector in the direction of the field $\mathbf{B}_n^m(x,y)$ which is tangential to the radial line from the n-th filament to (x,y), whereas $\rho_n^2(x,y) = (nD-x)^2 + y^2$. The mirror magnetic field becomes

$$\mathbf{B}^m(x,y) = \sum_{n=-\infty}^{\infty} \mathbf{B}_n^m(x,y) \tag{91}$$

$$= \frac{\mu_0}{4\pi}\sum_{n=-\infty}^{\infty} \frac{i_n^{rung}\hat{\mathbf{e}}_{\theta n}(x,y)}{\rho_n(x,y)}\zeta_n(w,x,y,z), \tag{92}$$

where $\zeta_n(w \longrightarrow \infty, x, y, z) = 2$, representing an infinitely wide track. Notice that (91) is periodic in the propulsion direction as $\mathbf{B}^m(x+D,y) = \mathbf{B}^m(x,y)$ from the shift invariance of the track. By resolving $\hat{\mathbf{e}}_{\theta n}(x,y)/\rho_n(x,y)$, using (90), and substituting $x = v^x t$ since we are interested in the time-varying part of $\mathbf{B}^m$ in the moving reference frame, (92) becomes

$$\mathbf{B}^m(t,y,z) = B'\frac{\mu_0}{4\pi}4\sin^2(\pi\tfrac{D}{\lambda}) \tag{93}$$

$$\sum_{n=-\infty}^{\infty}\left[\frac{1}{(nD-v^x t)^2 + y^2}\left(-y\hat{\mathbf{e}}_x + (nD - v^x t)\,\hat{\mathbf{e}}_y\right)\right. \tag{94}$$

$$\left(\frac{\frac{w}{2}-z}{\sqrt{(nD-v^x t)^2 + y^2 + \left(\frac{w}{2}-z\right)^2}} + \frac{\frac{w}{2}+z}{\sqrt{(nD-v^x t)^2 + y^2 + \left(\frac{w}{2}+z\right)^2}}\right) \tag{95}$$

$$\left.\sin(kv_x t - \pi\tfrac{D}{\lambda}(2n-1))\right], \tag{96}$$

where line (95) equals $\zeta_n(w,x,y,z)$.

Since the magnetic field is strongest at the transverse center, we set $z = 0$ and consider the magnitude $|\mathbf{B}^m(t,y)| = \frac{\mu_0}{4\pi}B' 4\sin^2(\pi\frac{D}{\lambda})\,|b(t)|$, where $b(t+T^D) = b(t)$ is periodic in $T^D \triangleq D/v^x$ and becomes

$$\begin{aligned} b(t) &= \left|\sum_{n=-\infty}^{\infty}\frac{1}{\sqrt{(nD-v^x t)^2 + y^2}}\frac{w}{\sqrt{(nD-v^x t)^2 + y^2 + \left(\frac{w}{2}\right)^2}}\right. \\ &\quad \left.\sin(kv_x t - \pi\tfrac{D}{\lambda}(2n-1))\right|, \end{aligned} \tag{97}$$

which is plotted in Figure 12. Notice that v^x does not influence the shape of $b(t)$, but only the scaling of the time axis.

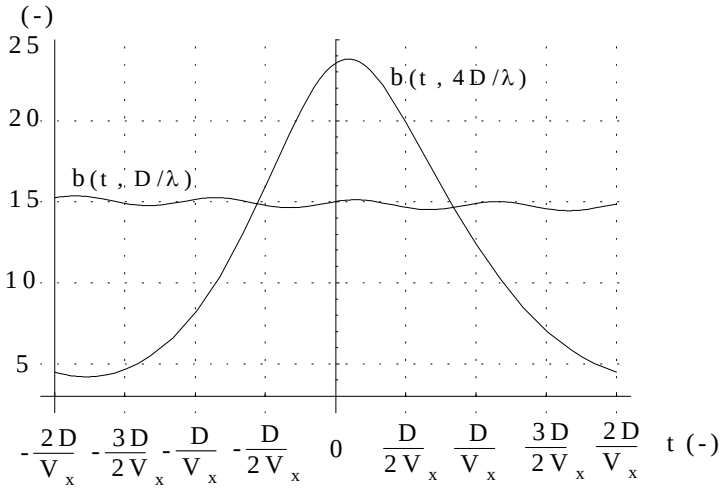

Figure 12: The function $b(t)$ plotted for D/λ and $4D/\lambda$. The parameter values are taken from General Magnetics' test wheel facility, and are: $\lambda = 0.4385\ m$, $D = 39.27\ mm$, and $w = 0.5\ m$, $y = 3\ cm$ and $z = 0\ cm$. Observe how the time-varying part decreases rapidly as D/λ is reduced.

We now separate $b(t)$ into a constant part $b^0 = \frac{1}{T^D}\int_{T^D} |b(t)|\, dt$ and a zero mean time-varying part $b^t(t) = b(t) - b^0$. Since $b^t(t)$ is not monochromatic, i.e. its Fourier series $b(\Omega_n)$ is nonzero for more than one frequency Ω_n, we have to introduce a norm to measure the size of the time-varying part relative to the time-invariant part. We choose the T^D-normalized $\mathcal{L}^1$-norm $\|b(t)\|_{\mathcal{L}^1(T^D)} \triangleq \frac{1}{T^D}\int_{T^D} |b(t)|\, dt$ for this purpose. By computing b^0 and $b^t(t)$ for physical feasible parameter values of y, z, w, D and λ, we infer that for $\pi D/\lambda \leq 1$ (representing densely spaced tracks)

$$\frac{\|b^t\|_{\mathcal{L}^1(T^D)}}{\|b^0\|_{\mathcal{L}^1(T^D)}} = \frac{\|b^t\|_{\mathcal{L}^1(T^D)}}{|b^0|} \sim \left(\frac{D}{\lambda}\right)^{\alpha}, \quad \alpha > 2 \tag{98}$$

For the two cases displayed in Figure 12, (98) is satisfied with $\alpha = 2.69$. By retaining the lowest order terms in D/λ of the factor in (93), we obtain $\sin^2(\pi\frac{D}{\lambda}) \sim (\pi\frac{D}{\lambda})^2$. Since the purely time-varying part of $|\mathbf{B}^m(t)|$ can be written as $|\mathbf{B}^m(t)| - \frac{1}{T^D}\int_{T^D} |\mathbf{B}^m(t)|\, dt$, we have a lower bound on the growth rate of the time-varying mirror magnetic field in the moving frame in the $\mathcal{L}^1$-norm as

$$\left\| |\mathbf{B}^m(t)| - \frac{1}{T^D}\int_{T^D} |\mathbf{B}^m(t)|\, dt \right\|_{\mathcal{L}^1(T^D)} < \gamma \left(\frac{D}{\lambda}\right)^4, \quad \text{for } \pi\frac{D}{\lambda} \leq 1, \tag{99}$$

where γ is a constant. We refer to (99) by saying that the time-varying mirror magnetic field in the moving reference frame is proportional to $(D/\lambda)^4$ for densely spaced tracks.

References

[1] W. Xiangming, "Achievements of Shanghai maglev demonstration operation line and the maglev development strategy," in *The 18th International Conference on Magnetically Levitated Systems and Linear Drives, (MAGLEV'2004)*, (Shanghai, China.), pp. 13–6, Oct, 26-28 2004.

[2] http://www.transrapid.de. Transrapid International, A Joint Company of Siemens and ThyssenKrupp.

[3] J. C. Maxwell, *A Treatise on Electricity and Magnetism*, vol. 2. New York: Dover, 3 ed., 1954. Unabridged, unaltered republication of the 3. edition published in 1891.

[4] B. V. Jayawant, *Electromagnetic Levitation and Suspension Techniques*. London, U.K.: Edward Arnold Publishers, 1981.

[5] J. R. Powell and G. T. Danby, "High speed transport by magnetically suspended trains," *ASME Winter Annual Meeting, New York, paper no. 66-WA/RR-5*, Nov. 27-Dec. 1 1966.

[6] J. R. Powell and G. T. Danby, "A 300-mph magnetically suspended train," *Mechanical Engineering*, vol. 89, p. 30, Nov. 1967.

[7] J. R. Powell and G. T. Danby, "Magnetically suspended trains: The application of superconductors to high speed transport," *Cryogenics & Industrial Gases*, vol. 4, pp. 19–24, Oct. 1969.

[8] J. R. Powell and G. T. Danby, "Magnetic suspension for levitated tracked vehicle," *Cryogenics*, pp. 192–204, 1971.

[9] H. G. Gutberlet, "The German magnetic transportation program," *IEEE Transactions on magnetics*, vol. MAG-10, pp. 417–20, Sep. 1974.

[10] L. Urankar, "Survey of basic magnetic levitation research in Erlangen," *IEEE Transactions on Magnetics*, vol. MAG-10, pp. 421–4, Sep, 1974.

[11] H. H. Kolm, R. D. Thornton, Y. Iwasa, and W. S. Brown, "The Magneplane system," *Cryogenics*, vol. 15, pp. 377–84, July 1975.

[12] R. H. Borcherts, "Repulsion magnetic suspension research – U.S. progress to date," *Cryogenics*, vol. 15, pp. 385–393, July 1975.

[13] Y. Kyotani, "Development of superconducting levitated trains in Japan," *Cryogenics*, vol. 15, pp. 372–6, July 1975.

[14] D. L. Atherton and A. R. Eastham, "Canadian developments in superconducting maglev and linear synchronous motors," *Cryogenics*, vol. 15, pp. 395–402, July 1975.

[15] R. Rhodes, B. Mulhall, J. Howell, and E. Abel, "The Wolfson maglev project," *IEEE Transactions on Magnetics*, vol. MAG-10, pp. 398–401, Sep. 1974.

[16] http://www.rtri.or.jp. Railway Technical Research Institute (RTRI) of Japan.

[17] S. Miyamoto, Y. Osada, K. Yamazumi, and T. Furuki, "The status of the running tests of JR-maglev," in *The 18th International Conference on Magnetically Levitated Systems and Linear Drives, (MAGLEV2004)*, (Shanghai, China), pp. 60–64, Oct. 26-28 2004.

[18] M. Sagawa, S. Fujimura, N. Togawa, H. Yamamoto, and Y. Matsuura, "New material for permanent magnets on a base of Nd and Fe (invited)," *Journal of Applied Physics*, vol. 55, pp. 2083–7, March 1984. Invited paper on NdFeB from the manufacturer of NEOMAX.

[19] Y. Kaneko, "Highest performance of Nd-Fe-B magnet over 55 MGOe," *IEEE Transactions on Magnetics*, vol. 36, pp. 3275–3278, Sept. 2000.

[20] J. C. Mallinson, "One-sided fluxes - a magnetic curiosity?," *IEEE Transactions on Magnetics*, vol. MAG-9, pp. 678–82, Dec. 1973. Origninal publication of one-sided fluxes.

[21] H. A. Shute, J. C. Mallinson, D. T. Wilton, and D. J. Mapps, "One-sided fluxes in planar, cylindrical, and spherical magnetized structures," *IEEE Transactions on Magnetics*, vol. 36, pp. 440–451, March 2000. Errata published in same Journal: Vol. 36, Issue 6, Nov. 2000, p. 4050.

[22] K. Halbach, "Fields and first order perturbation effects in two-dimensional conductor dominated magnets," *Nuclear Instruments and Methods*, vol. 78, pp. 185–97, 1970.

[23] K. Halbach, "Physical and optical propperties of rare earth cobalt magnets," *Nuclear Instruments and Methods*, no. 187, pp. 109–17, 1981.

[24] K. Halbach, "Applications of permanent magnets in accelerators and electron storage rings," *Journal of Applied Physics*, vol. 57, pp. 3605–8, April 1985.

[25] R. F. Post and D. D. Ryutov, "The Inductrack: A simpler approach to magnetic levitation," *IEEE Transactions on Applied Superconductivity*, vol. 10, pp. 901–904, March 2000.

[26] R. F. Post and D. D. Ryutov, "The Inductrack concept: A new approach to magnetic levitation," Tech. Rep. UCRL-ID-124115, Lawrence Livermore National Laboratory, May, 1996.

[27] W. A. Jacobs, "Magnetic launch assist – NASA's vision for the future," *IEEE Transactions on Magnetics*, vol. 37, pp. 55–57, Jan. 2001.

[28] P. L. Richards and M. Thinkham, "Magnetic suspension and propulsion systems for high-speed transportation," *Journal of Applied Physics*, vol. 43, pp. 2680–91, June 1972.

[29] R. Kratz and R. F. Post, "A null-current electro-dynamic levitation system," *IEEE Transactions on Applied Superconductivity*, vol. 12, pp. 930–932, March 2002.

[30] H. Gurol, B. Baldi, and R. F. Post, "Low speed maglev technology development program," Final Report U.S. Federal Transit Administration report no: FTA-CA-26-7025-02.1, U.S. National Technical Information Sevice (NTIS) Rep. no: PB2002105392, General Atomics, San Diego, California, March 2002.

[31] S. Gurol, R. Baldi, and D. Bever, "Status of the General Atomics low speed urban maglev technology development program," in *The 18th International Conference on Magnetically Levitated Systems and Linear Drives, (MAGLEV2004)*, (Shanghai, China), pp. 269–74, Oct. 26-28 2004.

[32] Communication with General Atomics.

[33] F. C. Moon, *Superconductive Magnetic Levitation: Applications to Bearings and Magnetic Transportation.* John Wiley & Sons, 1994.

[34] L. Hannakam, "Wirbelströme in dünnen leitytenden Platten infolge bewegter stromdurchflossener Leiter (Eddy currents in thin conducting sheets under a moving current carrying conductor)," *Elektrotechnische Zeitscrift A*, vol. 86, pp. 427–31, 1965.

[35] W. R. Smythe, *Static and Dynamic Electricity.* New York, USA: McGraw-Hill, 1939.

[36] A. V. Baiko, K. Voevodskii, and V. M. Kochetkov, "Vertical unstable stability of electrodynamic suspension of high-speed ground transport," *Cryogenics*, vol. 20, pp. 271–6, 1980.

[37] K. Higashi, S. Ohashi, H. Ohsaki, and E. Masada, "Magnetic damping of the electrodynamic suspension-type superconducting levitation system," *Electrical Engineering in Japan*, vol. 127, pp. 49–60, July-Aug. 1999. English Translation of Denki Gakkai Ronbunshi, vol. 117D, no. 8, Aug. 1997, pp. 1015-23.

[38] S. D. Lindenbaum and M. S. Lee, "Lift, drag and guidance forces on alternating polarity magnets, using loop guideways," *Journal of Applied Physics*, vol. 46, pp. 3151–9, July 1975.

[39] C. A. Guderjahn, S. L. Wipf, H. F. Fink, R. N. Boom, K. E. MacKenzie, D. Williams, and T. Downey, "Magnetic suspension and guidance for high speed rockets by superconducting magnets," *Journal of Applied Physics*, vol. 40, pp. 2133–40, April 1969.

[40] J. Y. Wong, B. E. Mulhall, and R. G. Rhodes, "The impedance modelling technique for investigating the characteristics of electrodynamic levitation systems," *Journal of Physics D: Applied Physics*, vol. 8, pp. 1948–55, Nov. 1975.

[41] Y. Iwasa, "Electromagnetic flight stability by model impedance simulation," *Journal of Applied Physics*, vol. 44, pp. 858–62, Feb. 1973.

[42] J. L. He, D. M. Rote, and H. T. Coffey, "Applications of the dynamic circuit theory to maglev suspension systems," *IEEE Transactions on Magnetics*, vol. 29, pp. 4153–64, Nov. 1993.

[43] O. P. Jain and B. T. Ooi, "The validity and the limitations of the AC impedance-modeling technique in electrodynamic levitation systems," *IEEE Transactions on Magnetics*, vol. MAG-15, pp. 1169–74, July 1979.

[44] *The 18th International Conference on Magnetically Levitated Systems and Linear Drives, (MAGLEV2004)*, (Shanghai, China), Oct. 26-28 2004.

[45] L. Urankar, "Intrinsic damping in basic magnetic levitation systems with a continuous sheet track," *Siemens Reaserch and Development Reports*, vol. 5, pp. 110–9, 1976.

[46] D. L. Atherton and A. R. Eastham, "Flat guidance schemes for magnetically levitated high-speed guided ground transport," *Journal of Applied Physics*, vol. 45, pp. 1398–405, March 1974.

[47] E. H. Brandt, "Levitation in physics," *Science*, vol. 243, pp. 349–55, Jan. 1989.

[48] O. F. Storset and B. E. Paden, "Dynamics of electrodynamic maglev," *Journal of Dynamic Systems, Measurement and Control.*, 2005. Submitted.

[49] M. T. Thompson and R. D. Thornton, "Flux-canceling electrodynamic maglev suspension: Part I test fixture design and modeling," *IEEE Transactions on Magnetics*, vol. 35, no. 3, pp. 1956–63, 1999.

[50] J. Miericke and L. Urankar, "Theory of electrodynamic levitation with a continuous sheet track - part I," *Applied Physics by Springer Verlag*, vol. 2, pp. 201–11, Oct. 1973.

[51] W. M. Saslow, "Maxwell's theory of eddy currents in thin conducting sheets, and applications to electromagnetic shielding and MAGLEV," *American Journal of Physics*, vol. 60, pp. 693–711, Aug. 1992.

[52] L. Urankar and J. Miericke, "Theory of electrodynamic levitation with a continuous sheet track - part II," *Applied Physics (Springer)*, vol. 3, pp. 67–76, Jan. 1974.

[53] T. K. Hunt, "AC losses in superconducting magnets at low excitation levels," *Journal of Applied Physics*, vol. 45, pp. 907–13, Feb. 1974.

[54] H. Ohsaki, H. Deguchi, and E. Masada, "Dynamical behavior analysis of the superconducting magnets for an EDS-LSM maglev," *International Journal of Applied Electromagnetics in Materials*, vol. 2, pp. 265–73, Dec. 1991.

[55] J. R. Reitz and L. C. Davis, "Force on a rectangular coil moving above a conducting slab," *Journal of Applied Physics*, vol. 43, pp. 1547–53, April 1972. Solves the field diffusion equation for abritary thickness, infinite extent, continuous track in Fourier domain.

[56] J. Langerhole, "Torques and forces on a moving coil due to eddy currents," *Journal of Applied Physics*, vol. 44, pp. 1587–94, April 1973.

[57] H. Hieronymus, J. Miericke, F. Pawlitschek, and M. Rudel, "Experimental study of magnetic forces on normal and null flux coil arrangements in the inductive levitation system," *Applied Physics, Springer Verlag*, vol. 3, no. 5, pp. 359–66, 1974.

[58] J. L. Boulnois and J.-L. Giovachini, "The fundamental solution in the theory of eddy currents and forces for conductors in steady motion," *Journal of Applied Physics*, vol. 49, pp. 2241–9, April 1978.

[59] B. T. Ooi and A. R. Eastham, "Transverse edge effects of sheet guideways in magnetic levitation," *IEEE Transactions on Power Apparatus & Systems*, vol. PAS-94, pp. 72–80, Jan.-Feb. 1975.

[60] L. Urankar, "Electrodynamics of finite width guideway maglev systems in an integral equation formulation," *Siemens Research and Development Reports*, vol. 8, no. 4, pp. 204–8, 1979.

[61] J.-L. Giovachini, "Green's function theory of eddy currents and forces for conductors in unsteady motion with application to electrodynamic levitation," *Journal of Applied Physics*, vol. 84, pp. 6426–39, Dec. 1998.

[62] K. Glatzel, G. Khurdok, and D. Rogg, "The development of the magnetically suspended transportation system in the federal republic of germany," *IEEE transactions on vehicular technology*, vol. VT-19, pp. 3–17, 1980.

[63] L. O. Hoppie, F. Chilton, H. T. Coffey, and R. C. Singleton, "Electromagnetic lift and drag forces on a superconducting magnet propelled along a guideway composed of metallic loops," *Proceedings of the 5th Applied Superconductivity Conference, Annapolis, MD (USA)*, p. 113, 1972.

[64] H. T. Coffey, F. Chilton, and L. O. Hoppie, "The feasibility of magnetically levitating high speed ground vehicles," Final Report, Task I U S National Technical Inormation Service Publication nb. 210 505, US Federal Railroad Administration Report no. PB 210 505, Stanford Research Institute, Menlo Park, California 94025, USA, February 1972. Identical to NTIS PB 221696.

[65] T. Yamada, M. Iwamoto, and T. Ito, "Levitation performance of magnetically suspended high speed trains," *IEEE Transactions on Magnetics*, vol. MAG-8, pp. 634–5, Sep. 1972.

[66] I. Takano, Y. Saito, and H. Ogiwara, "End effect of a magnetically suspended ultrahigh-speed train," *Transactions of the Institute of Electrical Engineers of Japan*, vol. 95, Jan.-Feb. 1975.

[67] E. Ohno, M. Iwamoto, and T. Yamada, "Characteristics of superconductive magnetic suspension and propulsion for high-speed trains," *Proceedings of the IEEE*, vol. 61, pp. 579–86, May 1973.

[68] T. Iwahana, "Study of superconducting magnetic suspension and guidance characteristics on loop tracks," *IEEE Transactions on Magnetics*, vol. MAG-11, pp. 1704–11, Nov. 1975.

[69] S. Nonaka, T. Hirosaki, and E. Kawakami, "Analysis of characteristics of repulsive magnetic levitated train using a space harmonic technique.," *Electrical Engineering in Japan (USA)*, vol. 100, pp. 80–8, Sept.-Oct. 1980. Translated from Denki Gakkai Ronbunshi, vol. 100B, n0. 10, Oct. 1980, pp. 601-608.

[70] N. Carbonari, G. Martinelli, and A. Morini, "Calculation of levitation, drag and lateral forces in EDS-MAGLEV transport systems," *Archiv fur Elektrotechnik*, vol. 71, no. 2, pp. 139–48, 1988.

[71] M. Andriollo, G. Martinelli, M. F. Moisio, and A. Morini, "Calculation of propulsion forces in EDS-maglev transport systems with superconducting coils," *Archiv fur Elektrotechnik*, vol. 72, no. 5, pp. 333–9, 1989.

[72] J. L. He, H. T. Coffey, and D. M. Rote, "Analysis of the combined maglev levitation, propulsion, and guidance system," *IEEE Transactions on Magnetics*, vol. 31, pp. 981–7, March 1995.

[73] S. Ohashi, H. Ohsaki, and E. Masada, "Equivalent model of the side wall electrodynamic suspension system," *Electrical Engineering in Japan (English Translation of Denki Gakkai Ronbunshi)*, vol. 124, pp. 63–73, July 1998.

[74] I.-K. Kim, R. Kratz, and D. Doll, "General Atomics urban maglev technology development," in *17th International Conference on Magnetically Levitated Systems and Linear Drives (MAGLEV'2002)*, (Lausanne, Switzerland), Sep. 3-5, 2002.

[75] D. Doll, R. D. Blevins, and D. Bhadra, "Ride DYnamics of general atomics' urban maglev," in *17th International Conference on Magnetically Levitated Systems and Linear Drives (MAGLEV'2002)*, (Lausanne, Switzerland), Sep. 3-5, 2002.

[76] D. W. Doll, R. Kratz, M. J. Newman, A. B. Plunkett, and R. D. Blevins, "Linear synchronous motor control for an urban maglev," in *The 18th International Conference on Magnetically Levitated Systems and Linear Drives, (MAGLEV2004)*, (Shanghai, China), pp. 275–287, Oct. 26-28 2004.

[77] Sumitomoto Special Metals Co. Ltd. (Presently: Neomax Materials Co. Ltd.), *NEOMAX, Rare Earth Magnets*. Japan, 2002. http://www.neomax.co.jp.

[78] L. D. Landau and E. M. Lifshitz, *Mechanics*. Course of Theoretical Physics, Volume 1, Oxford: Butterworth-Heinemann, 3. ed., 1993.

[79] H. Baruh, *Analytical Dynamics*. Boston: WCB/McGraw-Hill, 1 ed., 1999.

[80] L. D. Landau and E. M. Lifshitz, *Electrodynamics of Continuous Media*, vol. 8 of *Course of Theoretical Physics*. Oxford, UK: Butterworth-Heinemann, 2 ed., 1984.

[81] T. Murai and H. Hasegawa, "Electromagnetic analysis of inductrack magnetic levitation," *Electrical Engineering in Japan*, vol. 142, no. 1, pp. 67–74, 2003. Translation of Denki Gakkai Ronbunshi, vol. 121D, no. 10, Oct. 2001, pp. 1049-54.

[82] O. F. Storset and B. Paden, "Infinite dimensional models for perforated track electrodynamic maglev," *41st IEEE Conference on Decision and Control*, pp. 842–847, Dec. 2002.

[83] J. A. Ferreira, "Analytical computation of AC resistance of round and rectangular litz wire windings," *IEE Proceedings-Electric Power Applications*, vol. 139, pp. 21–25, Jan. 1992.

[84] P. L. Dowell, "Effects of eddy currents in transformer windings," *Proceedings of IEE*, vol. 113, pp. 1387–1394, Aug 1966.

[85] F. Tourkhani and P. Viarouge, "Accurate analytical model of winding losses in round litz wire windings," *IEEE Transactions on Magnetics*, vol. 37, pp. 538–43, Jan. 2001.

[86] C. R. Sullivan, "Cost-constrained selection of strand diameter and number in a litz-wire transformer winding," *IEEE Transactions on Power Electronics*, vol. 16, pp. 281 – 288, March 2001.

[87] C. R. Sullivan, "Optimal choice for number of strands in a litz-wire transformer winding," *IEEE Transactions on Power Electronics*, vol. 14, pp. 283 – 291, March 1999.

[88] A. D. Podoltsev, I. N. Kucheryavaya, and B. B. Lebedev, "Analysis of effective resistance and eddy-current losse in multiturn windings of high-frequency magnetic components," *IEEE Transactions on Magnetics*, vol. 39, pp. 539–48, Jan. 2003. Uses Homogenization of Maxwell's equations.

[89] F. W. Grover, *Inductance Calculations*. New York, USA: Dover Publications, 2004. Unabridged republication of the 1946 edition.

[90] D. M. Rote, "Passive damping in EDS maglev systems," in *17th International Conference on Magnetically Levitated Systems and Linear Drives (MAGLEV'2002), Lausanne, Switzerland*, (Lausanne, Switzerland), Sep. 3-5, 2002.